applied sciences

MDPI

Article

Improving Smartphone Pedestrian Positioning in Urban Canyons Through PDR-Constrained GNSS Shadow Matching

Nijia Qian [1], Xianggeng Han [1], Guobin Chang [1,2,*], Jingxiang Gao [1,*], Yu Cao [1], Yong Feng [1], Yueyang Huan [1], Yanlong Liu [1] and Haoran Liu [1]

[1] School of Environment and Spatial Informatics, China University of Mining and Technology, Xuzhou 221116, China; nijiaqian@cumt.edu.cn (N.Q.); ts23160005a31@cumt.edu.cn (X.H.); ts22160003a31@cumt.edu.cn (Y.C.); yongfeng@cumt.edu.cn (Y.F.); yueyanghuan@cumt.edu.cn (Y.H.); yanlongliu@cumt.edu.cn (Y.L.); liuhaoran@cumt.edu.cn (H.L.)
[2] State Key Laboratory of Spatial Datum, Xi'an 710054, China
* Correspondence: guobinchang@cumt.edu.cn (G.C.); jxgao@cumt.edu.cn (J.G.)

Featured Application

The proposed PDR-constrained GNSS shadow matching framework can be applied to reliable smartphone pedestrian positioning in dense urban environments where conventional GNSS positioning is degraded by building blockage, multipath, and non-line-of-sight reception. By integrating smartphone GNSS measurements, inertial-sensor-based pedestrian dead reckoning, and three-dimensional building models, the proposed approach can support location-based services such as pedestrian navigation, emergency response, intelligent transportation, and urban mobility applications without requiring dedicated high-grade positioning hardware.

Abstract

Smartphone global navigation satellite system (GNSS) positioning in building-obstructed environments is degraded by non-line-of-sight reception and multipath. Visibility-based shadow matching (SM) exploits three-dimensional building models to constrain cross-street position but has limited along-street observability. This study proposes a pedestrian dead reckoning (PDR)-constrained SM framework with two implementations: extended Kalman filter fusion (EKF-PDR/SM) using heading-orthogonal candidate search and anisotropic SM measurement uncertainty, and PDR-driven SM using candidate propagation, visibility scoring, and GNSS-proximity weighting. Evaluation used one smartphone and one pedestrian completing one traversal of each of two campus routes with different satellite-visibility conditions. Under common PDR prediction and process-noise settings, EKF-PDR/SM achieved cross-street/along-street root mean square errors (RMSEs) of 3.57/8.28 m on Route 1 and 2.46/7.83 m on Route 2, compared with 5.23/8.98 m and 4.29/12.38 m for EKF-PDR/GNSS, respectively. PDR-driven SM achieved the lowest directional RMSEs among the six compared methods: 2.92/7.47 m on Route 1 and 1.54/5.89 m on Route 2. All errors were evaluated relative to common model-derived reference trajectories. These controlled results support the use of PDR constraints to improve visibility-based SM under the tested conditions.

Keywords: smartphone positioning; GNSS shadow matching; pedestrian dead reckoning; urban canyon; GNSS/PDR integration; 3D building model; pedestrian navigation; multi-source fusion

Check for updates

Academic Editor: Ludovit Kovanic

Received: 25 September 2026
Revised: 28 October 2026
Accepted: 28 October 2026
Published: 29 October 2026

Copyright: © 2026 by the authors. Licensee MDPI, Basel, Switzerland. This article is an open access article distributed under the terms and conditions of the Creative Commons Attribution (CC BY) license.

1. Introduction

The rapid development of location-based services (LBS) has increased the demand for reliable pedestrian positioning in urban environments, with applications ranging from personal navigation and logistics to intelligent transportation and emergency response [1–3]. Smartphones have become one of the most widely used positioning platforms because they can provide absolute positioning through embedded global navigation satellite system (GNSS) chips and relative motion information through low-cost inertial sensors [4]. However, achieving stable and accurate smartphone positioning in dense urban canyons remains a challenging problem. The low-cost GNSS antennas and chipsets embedded in smartphones are highly sensitive to non-line-of-sight (NLOS) reception, multipath propagation, and signal blockage, which can introduce large biases into pseudorange single-point positioning (SPP) results [5–9]. Dual-frequency smartphone GNSS processing [10] and GPS/pseudolite integration [11] have been investigated for improving positioning performance. This study focuses on algorithmic integration of smartphone GNSS observations and inertial sensing for pedestrian positioning. Therefore, improving smartphone positioning performance through algorithmic and multi-source fusion approaches is of practical importance.

Shadow matching (SM) is an effective three-dimensional (3D) city model-aided GNSS positioning technique for urban canyons [12,13]. Instead of relying only on pseudorange measurements, SM uses the consistency between predicted satellite visibility at candidate positions and observed GNSS signal reception characteristics to infer the user's location. This visibility-based mechanism makes SM particularly useful for improving cross-street positioning, because satellite visibility patterns can vary substantially on opposite sides of a street [14]. However, SM has an inherent directional limitation. Along the street direction, neighboring candidate positions often share similar satellite visibility patterns, resulting in weak observability and limited along-street discrimination [14,15]. This problem becomes more significant in dynamic smartphone applications, where carrier-to-noise density ratio C/N_0 measurements used for visibility classification can fluctuate because of user motion, phone attitude changes, and local signal obstruction [16]. Consequently, standalone SM may improve the cross-street component of positioning while still producing large along-street errors or even road mismatching in challenging environments.

Considerable efforts have been devoted to improving SM and 3D model-aided GNSS positioning. Ray-tracing-based methods have been developed to model signal propagation paths and predict satellite visibility in complex urban environments [17]. Dynamic SNR thresholding, machine-learning-based line-of-sight/non-line-of-sight (LOS/NLOS) classification, and collaborative GNSS approaches have also been investigated to enhance satellite reception classification and mitigate NLOS effects [18–20]. For smartphone applications, SNR smoothing and locally optimized SM strategies have been proposed to improve the stability of visibility-based candidate scoring [16,21]. In addition, road network constraints and continuous SNR scoring have been introduced to reduce the candidate search space and improve positioning performance [21,22]. These studies have significantly advanced GNSS visibility-based positioning in urban canyons. Nevertheless, most existing improvements mainly rely on GNSS-derived information or 3D visibility constraints, and the along-street observability limitation of visibility-based SM has not been fully addressed, especially for dynamic pedestrian positioning with smartphones.

Pedestrian dead reckoning (PDR) provides a complementary information source for smartphone positioning. By detecting steps and estimating step length and heading from embedded inertial sensors, PDR can provide short-term relative displacement information independent of GNSS availability [23,24]. This capability makes PDR useful for maintaining positioning continuity when GNSS signals are degraded. However, PDR alone suffers from accumulated errors caused by step length uncertainty, heading drift, and phone attitude

variations. Therefore, PDR is usually integrated with absolute positioning information, such as GNSS SPP, through Kalman filtering, particle filtering, or factor graph optimization [24–27]. These GNSS/PDR fusion methods can improve pedestrian positioning under moderate GNSS conditions. However, when smartphone GNSS pseudorange positioning is severely affected by NLOS reception and multipath effects, direct fusion with raw GNSS SPP may introduce unreliable absolute updates into the PDR trajectory. This motivates the use of more environment-aware absolute constraints, such as 3D model-aided GNSS visibility information, in PDR fusion.

Several studies have explored the integration of dead reckoning, inertial sensing, and 3D map-aided GNSS positioning in urban environments. For example, SM has been extended to tightly coupled GNSS/INS integration for vehicle positioning [28], and smartphone-based dead reckoning has been integrated with 3D map-aided GNSS for urban pedestrian navigation [23]. Related studies have also demonstrated the effectiveness of multi-sensor integration for maintaining positioning continuity in challenging environments, including adaptive GNSS-RTK/LiDAR/IMU fusion in urban canyons [29] and BLE/PDR fusion for smartphone pedestrian positioning [30]. More recent studies have improved smartphone pedestrian positioning through PDR/GNSS integration using factor graph optimization, tightly coupled Bluetooth-enhanced GNSS/PDR fusion, and KF/FGO-based comparative frameworks [25–27]. These studies represent important directions for improving positioning continuity in degraded GNSS environments. However, they mainly focus on raw GNSS/PDR integration, ray-tracing-based or 3D map-aided GNSS positioning, additional radio measurements, or general sensor-fusion frameworks. The specific problem of how PDR information can be introduced into visibility-based smartphone SM, especially at the levels of candidate generation, candidate propagation, and candidate scoring, remains insufficiently investigated. This issue is important because visibility-based SM can be implemented using smartphone GNSS C/N_0 measurements and commonly available 3D building models without requiring full ray tracing or additional radio infrastructure.

This paper proposes a PDR-constrained GNSS shadow matching framework to improve smartphone positioning performance in urban canyons. Rather than simply combining PDR and SM as independent positioning solutions, this study exploits their complementary characteristics. Visibility-based SM provides useful cross-street constraints through 3D building-model-aided satellite visibility information, whereas PDR provides short-term trajectory information through step length and heading estimation. By integrating these complementary information sources, the proposed framework aims to reduce the directional errors of standalone SM and improve positioning stability under degraded GNSS conditions.

The main contributions of this paper are as follows:

1. A PDR-constrained visibility-based SM framework is developed for smartphone positioning in urban canyons. The framework integrates GNSS visibility information, smartphone inertial sensing, and road-constrained 3D model information to mitigate the directional limitations of standalone SM.
2. An extended Kalman filter (EKF)-based PDR/SM fusion method is proposed. In this method, the conventional area-based SM candidate search is replaced by a heading-orthogonal line-search strategy. PDR-derived heading information is used to constrain candidate generation, thereby improving candidate selection and reducing road mismatching.
3. A PDR-driven candidate update SM method is proposed. Candidate positions are dynamically propagated using PDR-derived step length and heading information, and the visibility-based SM score is coupled with a GNSS-proximity weighting term to enhance candidate discrimination while retaining the cross-street constraint provided by SM.

4. The proposed methods are evaluated through a controlled field experiment on two pedestrian routes representing different satellite visibility conditions. GNSS pseudorange SPP, standalone SM, EKF-PDR/GNSS, and PF-PDR/GNSS are used as baselines. All compared methods process the same smartphone observations and reference trajectories under fixed algorithmic settings, enabling a controlled assessment of the relative positioning performance under the tested urban-canyon conditions.

The remainder of this paper is organized as follows. Section 2 introduces the principles of visibility-based SM, smartphone PDR, and baseline PDR/GNSS fusion methods. Section 3 presents the proposed PDR-constrained SM framework, including the EKF-based PDR/SM fusion method and the PDR-driven candidate update SM method. Section 4 describes the experimental configuration and evaluates the positioning performance of different methods. Section 5 discusses the complementary characteristics of SM and PDR and the differences between the two proposed methods. Section 6 concludes the paper.

2. Positioning Principles and Baseline Methods

This section introduces the measurement principles and baseline methods used in this study. The visibility-based shadow matching (SM) measurement is first described, including candidate generation, road-constrained filtering, satellite visibility prediction and C/N_0-based scoring. The smartphone pedestrian dead reckoning (PDR) measurement model is then presented. Finally, two commonly used PDR/GNSS fusion strategies, namely extended Kalman filter (EKF)-based and particle filter (PF)-based PDR/GNSS integration, are introduced as baseline methods. These baselines are used to examine whether the SM-derived visibility measurement can provide a more reliable absolute constraint than raw GNSS pseudorange single-point positioning (SPP) in urban canyon environments.

To ensure a controlled comparison, all PDR-based methods use the same step detections, step-length estimates, heading observations, and synchronized smartphone measurements. In particular, the EKF-PDR/GNSS baseline and the proposed EKF-PDR/SM method share the same PDR prediction model and process-noise configuration. Their principal difference lies in the source of the absolute position update: raw GNSS SPP is used in EKF-PDR/GNSS, whereas the proposed method uses an SM-derived environment-aware position constraint. The PF-PDR/GNSS baseline uses the same PDR motion information and GNSS SPP observations but performs probabilistic particle propagation and weighting.

2.1. Visibility-Based Shadow Matching

Shadow matching is a three-dimensional (3D) city model-aided GNSS positioning method that estimates the receiver position by comparing predicted satellite visibility at candidate positions with observed GNSS signal reception characteristics [12,13]. In urban canyons, smartphone GNSS pseudorange measurements are often contaminated by non-line-of-sight (NLOS) reception, multipath propagation and signal blockage. Instead of directly relying on pseudorange residuals, visibility-based SM uses the spatial relationship among buildings, satellites and candidate receiver positions to infer the most likely user location. This mechanism makes SM particularly useful for constraining the cross-street component of pedestrian positioning in dense urban areas [14,15].

In this study, the locally optimized smartphone-based SM method is used as the basic visibility measurement model [21,22]. This method contains two important features. First, a continuous C/N_0-based scoring strategy is adopted so that the selected primary-frequency observation from each physical satellite contributes to candidate evaluation rather than being reduced to a binary LOS/NLOS classification. Second, road network constraints extracted from the 3D model are introduced to remove unreasonable candidate positions and reduce the possibility of locating the pedestrian outside the road area.

The workflow of the visibility-based SM measurement is illustrated in Figure 1. A GNSS-centred candidate region is first generated, as shown in Figure 1a. Road-constrained filtering is then applied to remove candidate positions outside the road area, as shown in Figure 1b. For each retained candidate position, a sky-view obstruction map is constructed from the 3D building model to predict satellite visibility, as shown in Figure 1c. The observed C/N_0 measurements are interpreted using the LOS and NLOS C/N_0 probability density functions shown in Figure 1d. Candidate positions are then scored according to the consistency between predicted visibility and observed C/N_0, as shown in Figure 1e. Finally, candidate positions satisfying the normalized score and road constraints are retained for weighted averaging, as shown in Figure 1f.

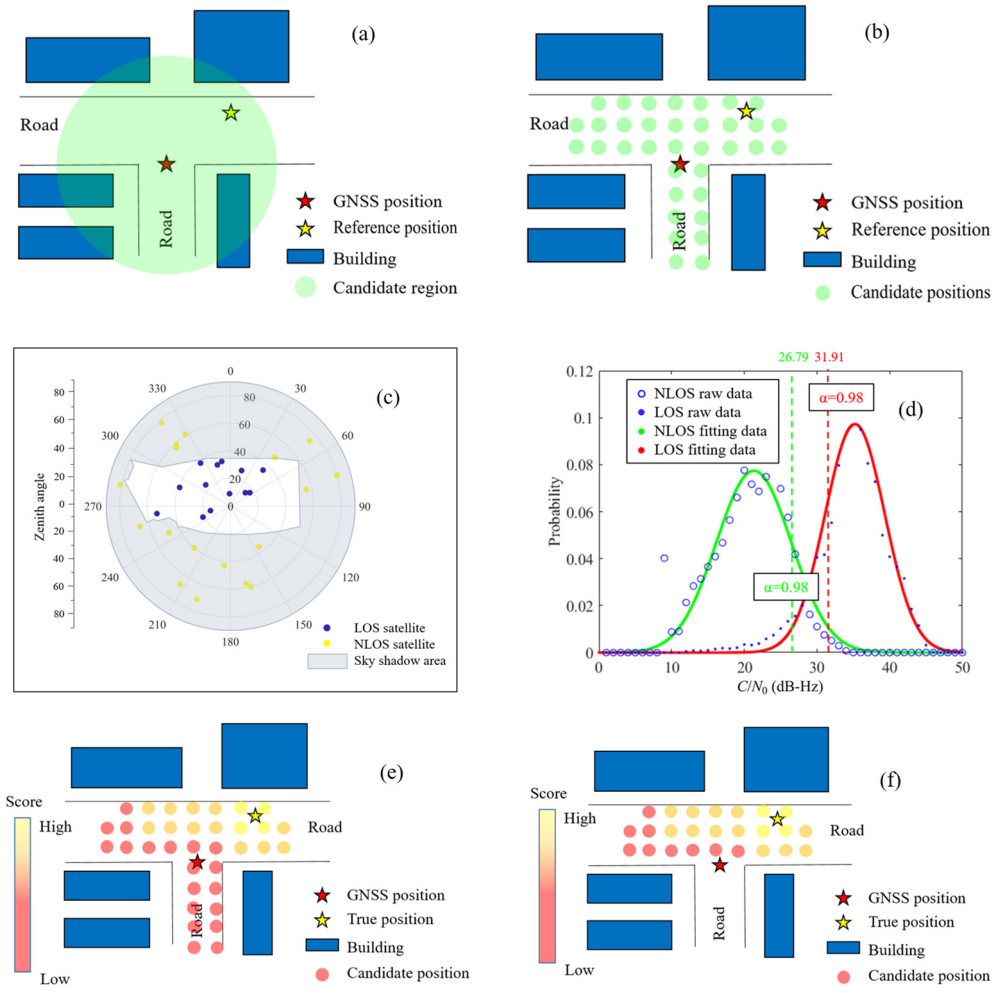


Figure 1. Workflow of the visibility-based shadow matching measurement: (**a**) definition of the GNSS-centred candidate search region; (**b**) road-constrained candidate positions after removing non-road candidates; (**c**) sky-view obstruction map constructed from the 3D building model; (**d**) LOS and NLOS C/N_0 probability density functions used for deriving the scoring thresholds; (**e**) visibility-consistency scores of candidate positions; (**f**) final retained candidate positions after score normalization and road-constrained filtering.

First, a candidate search region is initialized around the GNSS pseudorange SPP result. Let the GNSS SPP position at epoch i be denoted as

$$\boldsymbol{p}_i^{\mathrm{GNSS}} = \begin{bmatrix} E_i^{\mathrm{GNSS}} & N_i^{\mathrm{GNSS}} \end{bmatrix}^{\mathrm{T}} \tag{1}$$

where E and N are the east and north components in the local east-north-up coordinate frame. A circular candidate region is generated with $\boldsymbol{p}_i^{\mathrm{GNSS}}$ as the centre. In this study, the

initial candidate radius is set to 30 m, and candidate positions are sampled at 1 m intervals. The candidate set is expressed as

$$\boldsymbol{C}_i = \left\{ \boldsymbol{p}_{i,k} \middle| \left\| \boldsymbol{p}_{i,k} - \boldsymbol{p}_i^{\mathrm{GNSS}} \right\| \le R_{\mathrm{SM}} \right\} \tag{2}$$

where $\boldsymbol{P_{i,k}}$ denotes the k-th candidate position at epoch i, and R_{SM} is the candidate search radius.

Second, road-constrained filtering is performed using the road network information extracted from the 3D model. Candidate positions outside the road area are removed, and the road-constrained candidate set is given by

$$\boldsymbol{C}_i^{\mathrm{road}} = \left\{ \boldsymbol{p}_{i,k} \in \boldsymbol{C}_i \middle| \, \boldsymbol{p}_{i,k} \in \Omega_{\mathrm{road}} \right\} \tag{3}$$

where Ω_{road} denotes the road area derived from the 3D model. This step introduces spatial prior information into the positioning measurement and avoids unreasonable candidate positions located inside buildings or outside pedestrian-accessible areas.

Third, satellite visibility is predicted for each road-constrained candidate position. For each candidate position, the satellite azimuth and elevation angles are calculated from ephemeris data. Meanwhile, the local building obstruction boundary is constructed from the 3D model. A satellite is predicted as line-of-sight (LOS) if its elevation angle is higher than the building obstruction elevation in the corresponding azimuth direction; otherwise, it is predicted as NLOS. The predicted visibility state of satellite s at candidate position $\boldsymbol{p}_{i,k}$ can be written as

$$v_{i,k}^{s} = \begin{cases} 1, & \text{if satellite } s \text{ is predicted as LOS,} \\ 0, & \text{if satellite } s \text{ is predicted as NLOS.} \end{cases} \tag{4}$$

Fourth, the consistency between predicted satellite visibility and the smartphone-reported carrier-to-noise density ratio, C/N_0, is evaluated using the continuous scoring rule in Table 1. The lower and upper bounds, $c_{\mathrm{L}} = 26.79$ dB-Hz and $c_H = 31.91$ dB-Hz, follow the continuous scoring configuration reported in [22]. That reference established the bounds from LOS/NLOS signal-strength distributions using a nominal confidence level of 0.98. Both bounds are retained as fixed settings for the two experimental routes.

Table 1. Satellite scoring rules for visibility-based shadow matching.

Prediction	$\boldsymbol{C/N_0}$ **(dB-Hz)**		
	[0, 26.79)	**[26.79, 31.91)**	**[31.91, +∞)**
LOS	−1.0	$(C/N_0 - 29.35)/2.56$	1.0
NLOS	1.0	$(29.35 - C/N_0)/2.56$	−1.0

Let c denote the numerical C/N_0 value expressed in dB-Hz. For a satellite predicted as LOS, the score is −1 below the lower bound and +1 above the upper bound, with linear interpolation between the two bounds. For a satellite predicted as NLOS, the scoring signs are reversed. The midpoint and half-width of the transition interval are $(c_{\mathrm{L}} + c_H)/2 = 29.35$ dB-Hz and $(c_H - c_{\mathrm{L}})/2 = 2.56$ dB-Hz, respectively. Consequently, the transition scores are $(c - 29.35)/2.56$ for predicted LOS and $(29.35 - c)/2.56$ for predicted NLOS. This construction provides continuous, dimensionless scores between −1 and +1, with positive values indicating visibility consistency and negative values indicating inconsistency.

For the present multi-constellation processing, GPS, BDS, Galileo, and GLONASS observations were used. One primary-frequency observation was retained for each physical satellite at each epoch. Specifically, GPS L1 C/A, BDS B1I, Galileo E1, and GLONASS G1 were used for the visibility-based SM scoring. When additional frequencies from the same satellite were available, they were not treated as independent satellites in the SM

score. Accordingly, each physical satellite contributed at most one C/N_0 observation to the visibility-consistency score at a given epoch.

The total score of candidate position $\boldsymbol{p}_{i,k}$ is obtained by summing the satellite-level scores of all available satellites

$$S_{i,k} = \sum_{s=1}^{n_i} q\left(v_{i,k}^{s},\ C/N_{0,i}^{s}\right), \tag{5}$$

where $S_{i,k}$ is the visibility-consistency score of candidate position $\boldsymbol{p}_{i,k}$, n_i is the number of physical satellites retained for SM scoring at epoch i, $C/N_{0,i}^{s}$ is the selected carrier-to-noise density ratio of satellite s, and $q(\cdot)$ denotes the satellite-level scoring function defined in Table 1. At most one primary-frequency C/N_0 observation is used for each physical satellite.

Fifth, candidate scores are normalized to identify reliable candidate regions

$$\overline{S}_{i,k} = \frac{S_{i,k} - S_{i,\min}}{S_{i,\max} - S_{i,\min}}, \tag{6}$$

where $S_{i,\max}$ and $S_{i,\min}$ are the maximum and minimum candidate scores at epoch i, respectively. Candidate positions with min–max-normalized scores greater than 0.96 are retained; this threshold is fixed for both routes within the locally optimized SM framework [21,22].

Finally, the SM positioning measurement is calculated by a weighted average of the retained candidate positions

$$\boldsymbol{p}_i^{\mathrm{SM}} = \frac{\sum_{\boldsymbol{p}_{i,k} \in \boldsymbol{C}_i^{*}} \overline{S}_{i,k} \boldsymbol{p}_{i,k}}{\sum_{\boldsymbol{p}_{i,k} \in \boldsymbol{C}_i^{*}} \overline{S}_{i,k}}, \tag{7}$$

where $\boldsymbol{C}_i^{*}$ denotes the final retained candidate set after road-constrained filtering and score thresholding. The resulting $\boldsymbol{p}_i^{\mathrm{SM}}$ is used as the standalone SM positioning measurement. The effective weight of each retained candidate is its normalized visibility-consistency score divided by the sum of the normalized scores over $\boldsymbol{C}_i^{*}$, namely $w_{i,k} = \overline{S}_{i,k} / \sum_{\boldsymbol{p}_{i,j} \in \boldsymbol{C}_i^{*}} \overline{S}_{i,j}$. These weights are nonnegative and sum to one. Candidates excluded by the road constraint or score threshold receive zero weight in the final position estimate.

Although the visibility-based SM measurement can improve cross-street positioning by exploiting 3D building-model constraints, its along-street discrimination remains limited because candidate positions along the same street may have similar satellite visibility patterns. This directional limitation motivates the PDR-constrained SM methods proposed in Section 3.

2.2. Smartphone PDR

Pedestrian dead reckoning provides relative motion measurements using the embedded inertial sensors of a smartphone. Unlike GNSS measurements, PDR does not rely on satellite signal reception and can therefore maintain short-term positioning continuity in GNSS-degraded environments. In this study, PDR is used to provide step-length and heading measurements for constraining SM candidate generation, candidate propagation, and PDR-based state prediction. The PDR measurement principle is illustrated in Figure 2.

Let the pedestrian position at epoch i be

$$\boldsymbol{p}_i^{\mathrm{PDR}} = \begin{bmatrix} E_i^{\mathrm{PDR}} & N_i^{\mathrm{PDR}} \end{bmatrix}^{\mathrm{T}}. \tag{8}$$

The PDR position propagation model is expressed as

$$\begin{cases} E_{i+1}^{\mathrm{PDR}} = E_i^{\mathrm{PDR}} + L_i \sin\theta_i \\ N_{i+1}^{\mathrm{PDR}} = N_i^{\mathrm{PDR}} + L_i \cos\theta_i \end{cases}, \tag{9}$$

where L_i is the estimated step length between epochs i and $i+1$, and θ_i is the heading angle measured clockwise from the north direction. Here, i indexes successive step-propagation events, and L_i and θ_i describe the motion from $\boldsymbol{p}_i^{\mathrm{PDR}}$ to $\boldsymbol{p}_{i+1}^{\mathrm{PDR}}$. The same motion-input indexing convention is used in the EKF and PF propagation equations. The accuracy of PDR mainly depends on step detection, step length estimation and heading estimation.

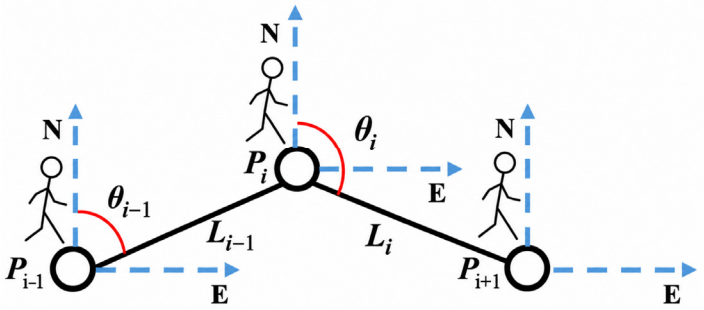


Figure 2. Smartphone PDR measurement principle. The step length L_i and heading θ_i describe the displacement from $\boldsymbol{p}_i$ to $\boldsymbol{p}_{i+1}$.

Step detection is performed using the magnitude of tri-axial accelerometer measurements. The acceleration magnitude at epoch i is calculated as

$$a_i = \sqrt{\left(a_i^x\right)^2 + \left(a_i^y\right)^2 + \left(a_i^z\right)^2}, \tag{10}$$

where a_i^x, a_i^y and a_i^z are the acceleration measurements along the three smartphone sensor axes. A peak-valley detection strategy is then used to identify walking steps from the acceleration magnitude sequence.

The step length is estimated using a Weinberg-type fourth-root model [31], applied to the acceleration-magnitude range defined from Equation (10)

$$L_i = K\sqrt[4]{a_i^{\max} - a_i^{\min}}. \tag{11}$$

Here, $a_i^{\max}$ and $a_i^{\min}$ are the maximum and minimum acceleration magnitudes within the corresponding detected step interval, and K is an empirical scale coefficient. The fourth-root relationship follows the Weinberg model [31]. The value $K = 0.408$ was inherited from the existing PDR implementation used in this study and retained as a fixed empirical setting. The same coefficient and acceleration-processing procedure were used for both routes and all PDR-based methods, providing common step-length inputs for the controlled comparison. The heading angle is obtained from the smartphone attitude and heading reference system (AHRS).

PDR provides useful along-trajectory displacement information, but its errors accumulate over time because of step-length uncertainty, heading error, and smartphone attitude variations. Therefore, PDR is not used as an independent positioning solution in this study. Instead, the PDR-derived step length L_i and heading θ_i are treated as control inputs for state propagation in both EKF-based methods and as motion inputs for candidate or particle propagation in the PDR-driven and PF-based methods. They are not included in the EKF state vector and are not treated as position observations in the measurement-update step.

2.3. EKF-Based PDR/GNSS Baseline

To evaluate whether the SM-derived visibility measurement can provide a more reliable environmental constraint than raw GNSS pseudorange SPP, an EKF-based PDR/GNSS fusion method is used as a baseline. The method uses PDR-derived step length and heading for state prediction and GNSS SPP as the absolute position observation.

The EKF state vector contains only the horizontal pedestrian position

$$\boldsymbol{x}_i = \begin{bmatrix} E_i & N_i \end{bmatrix}^{\mathrm{T}}, \tag{12}$$

where E_i and N_i are the east and north components in the local ENU coordinate frame.

The PDR-derived step length and heading are treated as control inputs rather than estimated states or measurement-update observations

$$\boldsymbol{u}_i = \begin{bmatrix} L_i & \theta_i \end{bmatrix}^{\mathrm{T}}, \tag{13}$$

where L_i and θ_i denote the step length and heading associated with pedestrian motion from epoch i to epoch $i+1$. Accordingly, the EKF does not estimate L_i or θ_i as state variables. Their uncertainties are instead propagated into the horizontal state covariance through the control-input Jacobian $\boldsymbol{G}_i$.

The nonlinear state-transition model is expressed as

$$\boldsymbol{x}_{i+1} = f(\boldsymbol{x}_i, \boldsymbol{u}_i) + \boldsymbol{w}_i \tag{14}$$

with

$$f(\boldsymbol{x}_i, \boldsymbol{u}_i) = \begin{bmatrix} E_i + L_i \sin\theta_i \\ N_i + L_i cos\theta \end{bmatrix}, \tag{15}$$

where $\boldsymbol{w}_i$ represents the process uncertainty arising primarily from errors in the PDR-derived step length and heading.

Because the horizontal position state enters the transition model additively, the state-transition Jacobian is $\boldsymbol{F}_i = \boldsymbol{I}_2$. The Jacobian with respect to the PDR control input is

$$\boldsymbol{G}_i = \frac{\partial f}{\partial \boldsymbol{u}_i} = \begin{bmatrix} \sin\theta_i & L_i \cos\theta_i \\ \cos\theta_i & -L_i sin\theta \end{bmatrix}. \tag{16}$$

The covariance of the PDR control-input errors is defined as

$$\boldsymbol{\Sigma}_{\boldsymbol{u}} = \begin{bmatrix} \sigma_L^2 & 0 \\ 0 & \sigma_\theta^2 \end{bmatrix}, \tag{17}$$

where the step-length and heading standard deviations are set to $\sigma_L = 0.10$ m and $\sigma_\theta = 5^\circ$ (0.0873 rad), respectively. The corresponding horizontal process-noise covariance is obtained by first-order uncertainty propagation

$$\boldsymbol{Q}_i = \boldsymbol{G}_i \boldsymbol{\Sigma}_{\boldsymbol{u}} \boldsymbol{G}_i^{\mathrm{T}}. \tag{18}$$

This formulation accounts for the uncertainty of the PDR-derived control inputs without augmenting either the state vector or the absolute-position measurement vector. The EKF prediction is then performed as

$$\hat{\boldsymbol{x}}_i^- = f\left(\hat{\boldsymbol{x}}_{i-1}^+, \boldsymbol{u}_{i-1}\right), \tag{19}$$

$$\boldsymbol{P}_i^- = \boldsymbol{F}_{i-1} \boldsymbol{P}_{i-1}^+ \boldsymbol{F}_{i-1}^{\mathrm{T}} + \boldsymbol{Q}_{i-1}. \tag{20}$$

The GNSS SPP result provides the absolute position observation

$$\boldsymbol{z}_i^{\mathrm{GNSS}} = \begin{bmatrix} E_i^{\mathrm{GNSS}} & N_i^{\mathrm{GNSS}} \end{bmatrix}^{\mathrm{T}}. \tag{21}$$

The observation model is

$$\boldsymbol{z}_i^{\mathrm{GNSS}} = \boldsymbol{H}\boldsymbol{x}_i + \boldsymbol{v}_i. \tag{22}$$

Because L_i and θ_i are control inputs, the GNSS measurement vector contains only the horizontal position components, and the observation matrix remains $\boldsymbol{H} = \boldsymbol{I}_2$. $\boldsymbol{v}_i$ denotes

the GNSS SPP observation noise. An isotropic GNSS measurement covariance $\boldsymbol{R}^{\mathrm{GNSS}} = \mathrm{diag}(10^2, 10^2)\ \mathrm{m}^2$ is adopted. The initial state is set to the first valid GNSS SPP position, and the initial covariance is $\boldsymbol{P}_0 = \mathrm{diag}(10^2, 10^2)\ \mathrm{m}^2$.

The update step is

$$\boldsymbol{K}_i = \boldsymbol{P}_i^- \boldsymbol{H}^{\mathrm{T}} \left(\boldsymbol{H} \boldsymbol{P}_i^- \boldsymbol{H}^{\mathrm{T}} + \boldsymbol{R}_{\mathrm{GNSS}} \right)^{-1}, \tag{23}$$

$$\hat{\boldsymbol{x}}_i^+ = \hat{\boldsymbol{x}}_i^- + \boldsymbol{K}_i \left(\boldsymbol{z}_i^{\mathrm{GNSS}} - \boldsymbol{H} \hat{\boldsymbol{x}}_i^- \right), \tag{24}$$

$$\boldsymbol{P}_i^+ = (\boldsymbol{I} - \boldsymbol{K}_i \boldsymbol{H}) \boldsymbol{P}_i^-. \tag{25}$$

For the controlled comparison in this study, EKF-PDR/GNSS and EKF-PDR/SM use exactly the same PDR measurements, state definition, initialization, and process-noise covariance $\boldsymbol{Q}_i$. Their principal difference lies in the absolute position observation: EKF-PDR/GNSS directly uses GNSS SPP with an isotropic measurement covariance, whereas EKF-PDR/SM uses the SM-derived position with a heading-dependent anisotropic measurement covariance, as described in Section 3.2.

2.4. PF-Based PDR/GNSS Baseline

A PF-based PDR/GNSS fusion method is also used as a nonlinear probabilistic baseline. Compared with the EKF, the PF represents the posterior distribution of the pedestrian state using a set of weighted particles and is therefore more flexible for nonlinear and non-Gaussian positioning problems.

At epoch i, the particle set is denoted as

$$\left\{ \boldsymbol{x}_i^{(m)}, w_i^{(m)} \right\}_{m=1}^{M}, \tag{26}$$

where $\boldsymbol{x}_i^{(m)}$ is the state vector of the m-th particle, $w_i^{(m)}$ is its weight, and M is the number of particles. In this study, M is set to 1000.

During initialization, particles are generated around the initial GNSS SPP position by adding random perturbations

$$\boldsymbol{x}_0^{(m)} = \boldsymbol{x}_0^{\mathrm{GNSS}} + \boldsymbol{e}_0^{(m)}, \tag{27}$$

where $\boldsymbol{e}_0^{(m)}$ denotes the initial sampling noise. The initial particle weights are set uniformly

$$w_0^{(m)} = \frac{1}{M}. \tag{28}$$

During state propagation, each particle is updated using the PDR motion model

$$\boldsymbol{x}_i^{(m)} = f\left(\boldsymbol{x}_{i-1}^{(m)}, \boldsymbol{u}_{i-1}^{(m)} \right), \tag{29}$$

where $\boldsymbol{u}_{i-1}^{(m)} = \left[L_{i-1}^{(m)}, \theta_{i-1}^{(m)} \right]^{\mathrm{T}}$ denotes the perturbed PDR control input of the m-th particle. The step-length and heading perturbations are modeled as zero-mean Gaussian variables with standard deviations of 0.10 m and 5°, respectively, consistent with the uncertainty settings adopted in the EKF-based methods.

After receiving the GNSS SPP measurement $\boldsymbol{z}_i^{\mathrm{GNSS}}$, the particle weight is updated according to the consistency between the particle position and the GNSS observation. A Gaussian likelihood model is used

$$\widetilde{w}_i^{(m)} = \widetilde{w}_{i-1}^{(m)} \exp\left[-\frac{1}{2} \left(\boldsymbol{z}_i^{\mathrm{GNSS}} - \boldsymbol{H} \boldsymbol{x}_i^{(m)} \right)^{\mathrm{T}} \boldsymbol{R}_i^{-1} \left(\boldsymbol{z}_i^{\mathrm{GNSS}} - \boldsymbol{H} \boldsymbol{x}_i^{(m)} \right) \right], \tag{30}$$

where $\widetilde{w}_i^{(m)}$ is the unnormalized particle weight. In the likelihood calculation, $\boldsymbol{R}_i = \boldsymbol{R}^{\mathrm{GNSS}} = \mathrm{diag}(10^2, 10^2)\ \mathrm{m}^2$, consistent with the GNSS measurement covariance used by EKF-PDR/GNSS. The weights are then normalized as

$$w_i^{(m)} = \frac{\widetilde{w}_i^{(m)}}{\sum_{j=1}^{M} \widetilde{w}_i^{(j)}}. \tag{31}$$

The estimated position is calculated by the weighted average of all particles

$$\hat{\boldsymbol{p}}_i^{\mathrm{PF-GNSS}} = \sum_{m=1}^{M} w_i^{(m)} \boldsymbol{p}_i^{(m)}, \tag{32}$$

where $\boldsymbol{p}_i^{(m)}$ denotes the horizontal position component of particle $\boldsymbol{x}_i^{(m)}$.

To reduce particle degeneracy, the effective sample size is calculated as

$$N_{\mathrm{eff}} = \frac{1}{\sum_{m=1}^{M} \left(w_i^{(m)}\right)^2}. \tag{33}$$

Systematic resampling is performed when $N_{\mathrm{eff}} < 0.5M$. Particles with larger weights are more likely to be retained, whereas particles with smaller weights are removed. The PF-based PDR/GNSS method is used as a second baseline because it represents a commonly used probabilistic fusion strategy for smartphone pedestrian positioning.

It should be noted that both the EKF-based and PF-based PDR/GNSS baselines directly use GNSS SPP as the absolute measurement update. Therefore, their performance strongly depends on the reliability of smartphone GNSS pseudorange positioning. In contrast, the proposed methods in Section 3 use SM-derived visibility measurements and PDR motion measurements jointly, aiming to provide a more environment-aware absolute constraint under degraded GNSS conditions.

3. PDR-Constrained Shadow Matching Methods

The methods introduced in Section 2 show that visibility-based SM and smartphone PDR have complementary measurement characteristics. SM can provide environment-aware absolute positioning information by using GNSS visibility measurements and 3D building-model constraints, but its along-street discrimination is weak because neighbouring positions along the same street often share similar satellite visibility patterns. In contrast, PDR can provide short-term along-trajectory displacement measurements through step length and heading estimation, but its errors accumulate over time without reliable absolute constraints. Therefore, this section develops two PDR-constrained SM methods to exploit the measurement complementarity between SM and PDR.

The first method is an EKF-based PDR/SM fusion method, in which the SM-derived position is used as an environment-aware measurement update and the SM candidate search is constrained using PDR-derived heading information. The second method is a PDR-driven candidate update SM method, in which candidate positions are propagated by PDR motion measurements and then evaluated using both SM visibility consistency and GNSS-proximity weighting. These two methods are designed to reduce along-street ambiguity and mitigate road-mismatching of standalone SM in dynamic smartphone positioning.

3.1. Overall PDR-Constrained SM Framework

Let $\mathcal{J}_i$ denote the set of detected steps occurring between consecutive GNSS epochs $t_{i\text{-}1}$ and t_i. The accumulated PDR displacement over this interval is expressed as

$$\Delta \boldsymbol{d}_i^{\mathrm{PDR}} = \sum_{j \in \mathcal{J}_i} L_j \begin{bmatrix} \sin\theta_j \\ \cos\theta_j \end{bmatrix}. \tag{34}$$

Here, L_j and θ_j are the estimated length and heading of detected step j, with heading measured clockwise from north. The displacement is zero when the interval contains no detected steps. This accumulated displacement is used for propagation between consecutive GNSS measurement epochs.

The key idea of the proposed framework is not to simply average the PDR and SM positioning results. Instead, PDR measurements are introduced into the SM process at the candidate level and measurement fusion level. Specifically, PDR-derived heading is used to constrain the direction of SM candidate generation in the EKF-based method, while PDR-derived step length and heading are used to propagate candidate positions in the PDR-driven SM method. In this way, PDR contributes to the along-street motion constraint, whereas SM retains its advantage in cross-street visibility discrimination.

The two proposed methods introduce PDR information into visibility-based SM at different integration levels. In the EKF-PDR/SM method, PDR is used in two stages. First, the PDR-derived heading constrains the SM candidate search to the heading-orthogonal direction, so that SM primarily extracts the cross-street information in which satellite visibility is most discriminative. Second, the PDR displacement provides the state prediction in the EKF, while the SM-derived position provides the environment-aware absolute position update. In contrast, the PDR-driven SM method does not perform a Kalman-filter or particle-filter state update. Instead, the candidate positions are directly propagated from epoch to epoch using the PDR-derived step length and heading. The propagated candidates are then evaluated using road constraints, SM visibility consistency, and GNSS-proximity weighting, and the final position is obtained by normalized weighted averaging. Therefore, the former method integrates PDR and SM at the measurement-update level, whereas the latter integrates them at the candidate-propagation and candidate-scoring level.

3.2. EKF-Based PDR/SM Fusion with Heading-Orthogonal Candidate Search

In conventional SM, candidate positions are usually generated within a two-dimensional search region centered on the GNSS SPP position. This area-based search is effective for identifying the correct side of the street, but it does not explicitly exploit pedestrian motion direction. Consequently, candidate positions distributed along the same street may exhibit similar satellite visibility patterns, resulting in weak along-street discrimination.

To address this limitation, the EKF-PDR/SM method introduces a heading-orthogonal candidate search strategy. Instead of generating candidate positions over a circular area, candidate positions are generated along a line perpendicular to the pedestrian heading. This design is based on the directional complementarity between PDR and SM: PDR provides short-term displacement information primarily along the walking direction, whereas SM provides stronger geometric discrimination in the cross-street direction through building-induced satellite visibility changes. Therefore, the SM candidate search is concentrated in the direction in which visibility information is most discriminative.

The heading-orthogonal candidate generation is illustrated in Figure 3a. A possible candidate-domain failure caused by heading deviation is shown in Figure 3b, the heading-smoothing effect is shown in Figure 3c, and the complete EKF-PDR/SM workflow is summarized in Figure 3d.

Let the GNSS SPP position at epoch i be $\boldsymbol{p}_i^{\mathrm{GNSS}}$, and let the smoothed pedestrian heading be $\tilde{\theta}_i$. Because the heading angle is measured clockwise from north, the unit vector along the pedestrian heading is defined as

$$\boldsymbol{u}_i^{\parallel} = \begin{bmatrix} \sin\tilde{\theta}_i \\ \cos\tilde{\theta}_i \end{bmatrix}, \tag{35}$$

and the corresponding heading-orthogonal unit vector is

$$\boldsymbol{u}_i^{\perp} = \begin{bmatrix} \cos\tilde{\theta}_i \\ -\sin\tilde{\theta}_i \end{bmatrix}. \tag{36}$$

The heading-orthogonal candidate set is then generated as

$$\boldsymbol{C}_i^{\perp} = \left\{ \boldsymbol{p}_{i,k} = \boldsymbol{p}_i^{\mathrm{GNSS}} + r_k \boldsymbol{u}_i^{\perp} \mid r_k \in [-R_{\perp}, R_{\perp}] \right\}, \tag{37}$$

where $R_{\perp}$ denotes the candidate search range in the heading-orthogonal direction. In this study, $R_{\perp}$ is set to 10 m, and candidate positions are generated at 1 m intervals. Candidates outside the pedestrian-accessible road area are removed using the road constraint described in Section 2.1.

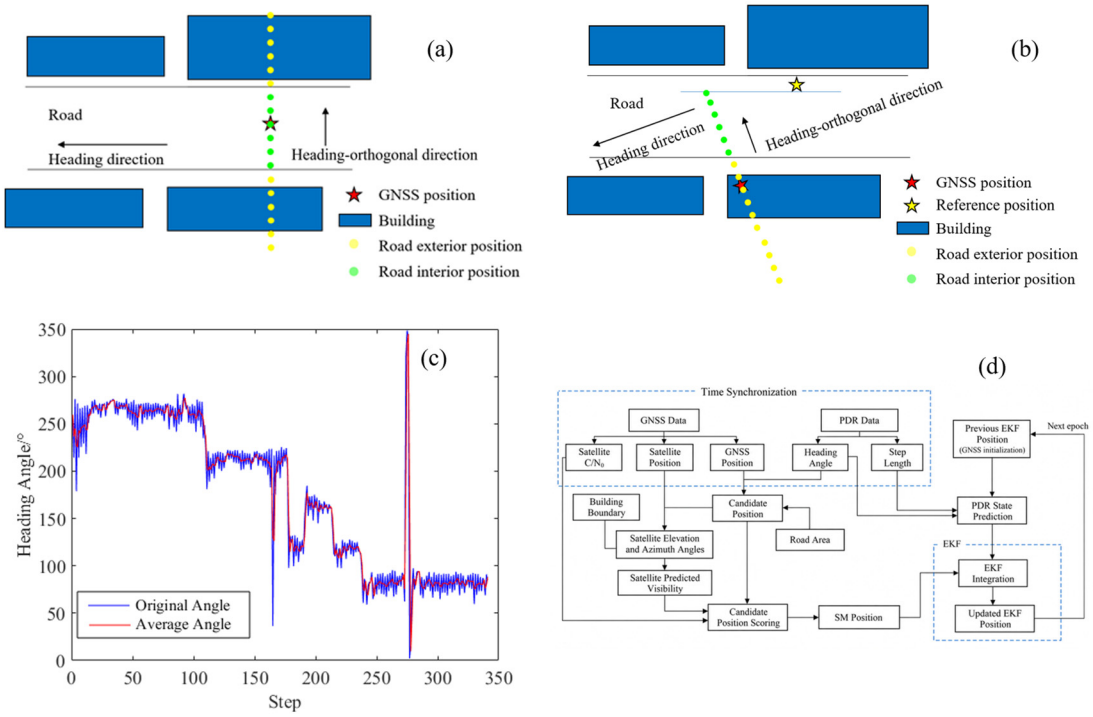


Figure 3. EKF-based PDR/SM fusion with heading-orthogonal candidate search: (**a**) heading-orthogonal candidate generation; (**b**) possible candidate-domain failure caused by heading deviation; (**c**) heading smoothing effect; (**d**) workflow of the EKF-based PDR/SM fusion method.

The raw heading obtained from the smartphone AHRS may fluctuate because of sensor noise, magnetic disturbance, and pedestrian motion. Such heading errors can rotate the heading-orthogonal search line away from the true cross-street direction and may consequently exclude valid candidate positions. Therefore, first-order heading smoothing is applied before candidate generation

$$\tilde{\theta}_i = \alpha_\theta \tilde{\theta}_{i-1} + (1 - \alpha_\theta)\theta_i, \tag{38}$$

where θ_i and $\tilde{\theta}_i$ are the raw and smoothed heading angles, respectively, and $\alpha_\theta = 0.8$ is the smoothing coefficient. Circular angle wrapping is applied when the heading crosses the 0°/360° boundary.

After the heading-orthogonal candidate set is generated, the visibility prediction, C/N_0-based scoring, score normalization, and weighted averaging procedures described in Section 2.1 are applied to $\boldsymbol{C}_i^{\perp}$. The resulting SM-derived position measurement is

$$\boldsymbol{z}_i^{\mathrm{SM}} = \begin{bmatrix} E_i^{\mathrm{SM}} & N_i^{\mathrm{SM}} \end{bmatrix}^{\mathrm{T}}. \tag{39}$$

The EKF-PDR/SM method uses exactly the same horizontal state definition, PDR control input, initialization, and process-noise model as the EKF-PDR/GNSS baseline described in Section 2.3. In both EKF methods, the state vector is $\boldsymbol{x}_i = [E_i, N_i]^{\mathrm{T}}$, while the

PDR-derived step length L_i and heading θ_i are treated exclusively as control inputs for state propagation. They are neither estimated state variables nor elements of the absolute-position measurement vector. Accordingly, both methods use the same PDR-derived state prediction and the same process-noise covariance Q_i. The difference between the two EKF methods lies in the absolute position measurement and its uncertainty model.

Because visibility-based SM exhibits substantially different observability in the along-heading and cross-heading directions, an isotropic measurement covariance is not appropriate for the SM update. The local heading-frame transformation matrix is defined as

$$\boldsymbol{C}_i = \begin{bmatrix} \sin\tilde{\theta}_i & \cos\tilde{\theta}_i \\ \cos\tilde{\theta}_i & -\sin\tilde{\theta}_i \end{bmatrix} = \begin{bmatrix} \boldsymbol{u}_i^{\parallel} & \boldsymbol{u}_i^{\perp} \end{bmatrix}. \tag{40}$$

In the local heading frame, the SM measurement covariance is defined as

$$\boldsymbol{R}_h^{\mathrm{SM}} = \begin{bmatrix} \sigma_{\parallel}^2 & 0 \\ 0 & \sigma_{\perp}^2 \end{bmatrix} = \begin{bmatrix} 20^2 & 0 \\ 0 & 5^2 \end{bmatrix} \mathrm{m}^2, \tag{41}$$

where $\sigma_{\parallel} = 20$ m and $\sigma_{\perp} = 5$ m denote the along-heading and cross-heading standard deviations, respectively. The substantially larger along-heading variance explicitly represents the weak along-street observability of visibility-based SM, whereas the smaller cross-heading variance allows the filter to exploit the stronger cross-street visibility constraint.

At each epoch, the SM covariance is transformed from the heading frame to the local EN frame according to

$$\boldsymbol{R}_i^{SM} = \boldsymbol{C}_i \boldsymbol{R}_h^{SM} \boldsymbol{C}_i^{T}. \tag{42}$$

The SM measurement equation is

$$\boldsymbol{z}_i^{\mathrm{SM}} = \boldsymbol{H}\boldsymbol{x}_i + v_i^{\mathrm{SM}}, \tag{43}$$

where $\boldsymbol{H} = \boldsymbol{I}_2$, v_i^{SM} denotes the SM measurement noise, and its covariance is $\boldsymbol{R}_i^{SM}$. The EKF measurement update is then performed as

$$\boldsymbol{K}_i = \boldsymbol{P}_i^{-}\boldsymbol{H}^{\mathrm{T}}\left(\boldsymbol{H}\boldsymbol{P}_i^{-}\boldsymbol{H}^{\mathrm{T}} + \boldsymbol{R}_i^{\mathrm{SM}}\right)^{-1}, \tag{44}$$

$$\hat{\boldsymbol{x}}_i^{+} = \hat{\boldsymbol{x}}_i^{-} + \boldsymbol{K}_i\left(\boldsymbol{z}_i^{\mathrm{SM}} - \boldsymbol{H}\hat{\boldsymbol{x}}_i^{-}\right), \tag{45}$$

and

$$\boldsymbol{P}_i^{+} = (\boldsymbol{I} - \boldsymbol{K}_i\boldsymbol{H})\boldsymbol{P}_i^{-}. \tag{46}$$

Therefore, EKF-PDR/GNSS and EKF-PDR/SM use identical PDR state prediction, initialization, and process-noise covariance. The EKF-PDR/GNSS baseline uses GNSS SPP as an isotropic absolute position observation, whereas EKF-PDR/SM uses an environment-aware SM observation with heading-dependent anisotropic uncertainty. This formulation assigns lower confidence to the SM observation along the heading direction while retaining a stronger cross-heading constraint.

In Figure 3d, PDR state prediction uses the previous EKF position together with the step-length and heading measurements. All detected step displacements between consecutive GNSS epochs are accumulated according to Equation (34). The first valid GNSS SPP position initializes the filter, and subsequent predictions start from the preceding EKF-updated position. The SM-derived position then provides the absolute-position measurement for the EKF update.

3.3. PDR-Driven Candidate Update Shadow Matching

The second proposed method introduces PDR measurements directly into the candidate update process of SM. Unlike the EKF-PDR/SM method, which calculates an SM measurement and then fuses it with PDR in a filtering framework, the PDR-driven SM method updates candidate positions at each epoch using PDR-derived step length and heading. Candidate positions are then evaluated by combining visibility consistency and GNSS-proximity information.

The initial candidate set is shown in Figure 4a, the PDR-driven candidate propagation process is illustrated in Figure 4b, and the complete workflow is presented in Figure 4c.

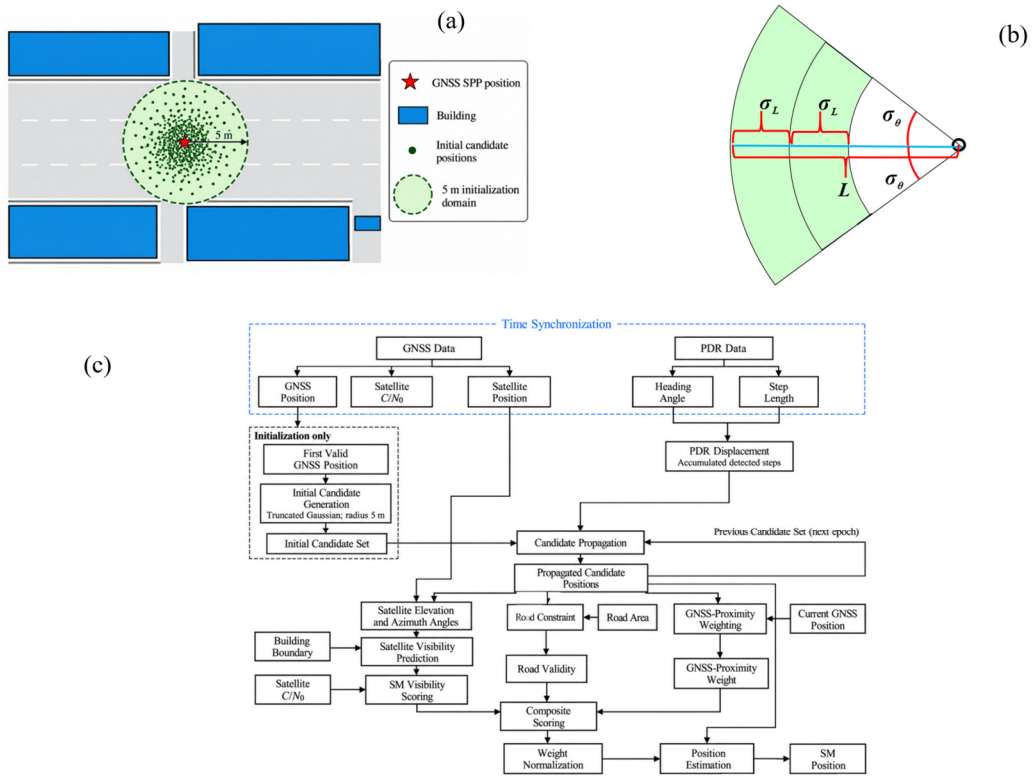


Figure 4. PDR-driven candidate update SM: (**a**) schematic illustration of the initial candidate set generated from a truncated two-dimensional Gaussian distribution centered on the GNSS SPP position and confined within a 5 m circular initialization domain (not drawn to geographic scale); (**b**) PDR-driven candidate propagation using step-length and heading measurements; (**c**) workflow showing candidate initialization, PDR-based candidate propagation, road and visibility evaluation, GNSS-proximity weighting, and position estimation.

At the initial epoch, the PDR-driven SM candidate set is generated around the first valid GNSS SPP position. The initial candidate set is defined as

$$\boldsymbol{C}_0^{\mathrm{PD}} = \left\{ \boldsymbol{p}_{0,k} \;\middle|\; \left\| \boldsymbol{p}_{0,k} - \boldsymbol{p}_0^{\mathrm{GNSS}} \right\|_2 \le R_{\mathrm{PD}}, \quad k = 1, 2, \ldots, M^{SM} \right\}, \tag{47}$$

where M^{SM} denotes the number of candidate positions and R_{PD} denotes the initial candidate radius. In this study, $M^{\mathrm{SM}} = 500$ and $R_{\mathrm{PD}} = 5$ m. The candidate positions are sampled from an isotropic two-dimensional Gaussian distribution centered on the first GNSS SPP position, with $\sigma_E = \sigma_N = 2.5$ m. A circular truncation constraint is then applied: any sampled candidate satisfying $\|\boldsymbol{p}_{0,k} - \boldsymbol{p}_0^{\mathrm{GNSS}}\|_2 > 5$ m is rejected and regenerated until 500 valid candidates are obtained. Consequently, every candidate in the initialized candidate set lies within 5 m of the GNSS SPP position.

The 5 m radius is applied only to candidate initialization. From the subsequent epoch onward, the candidate positions are propagated continuously from the previous candidate set using the PDR-derived displacement rather than being regenerated within a new 5 m GNSS-centered region.

After initialization, the candidate set is propagated recursively using the PDR displacement. For epoch i, each candidate position is updated as

$$\boldsymbol{p}_{i,k}^{-} = \boldsymbol{p}_{i-1,k}^{+} + \sum_{j \in \mathcal{J}_i} (L_j + \varepsilon_{j,k}^{L}) \begin{bmatrix} \sin(\theta_j + \varepsilon_{j,k}^{\theta}) \\ \cos(\theta_j + \varepsilon_{j,k}^{\theta}) \end{bmatrix}. \tag{48}$$

Here, $\mathcal{J}_i$ contains the steps detected between consecutive GNSS epochs t_{i-1} and t_i. For each candidate and detected step, independent perturbations are sampled as $\varepsilon_{j,k}^{L} \sim \mathcal{N}(0, \sigma_L^2)$ and $\varepsilon_{j,k}^{\theta} \sim \mathcal{N}(0, \sigma_\theta^2)$, with $\sigma_L = 0.10$ m and $\sigma_\theta = 5^\circ$. Angular quantities are converted to radians for computation. Equation (34) defines the nominal accumulated displacement, while Equation (48) incorporates the PDR input uncertainties into candidate propagation. The propagation displacement is zero when no steps are detected in the interval.

After candidate propagation, road constraints are applied. Candidate positions outside the road area are assigned zero score

$$S_{i,k}^{\text{road}} = \begin{cases} 1, & \boldsymbol{p}_{i,k}^{-} \in \Omega_{\text{road}} \\ 0, & \boldsymbol{p}_{i,k}^{-} \notin \Omega_{\text{road}} \end{cases}. \tag{49}$$

For each candidate inside the road area, the raw visibility-consistency score is calculated using the satellite-level C/N_0 scoring rule in Section 2.1. The raw scores are then transformed into nonnegative scores using the min–max normalization in Equation (6), evaluated over the current road-valid candidate set. The normalized visibility score is denoted by $\overline{S}_{i,k}^{\text{SM}}$. The comprehensive score combines this normalized visibility score with road validity and GNSS-proximity weighting.

To enhance along-street score discrimination, a GNSS-proximity weighting term is introduced. This term evaluates the spatial consistency between the propagated candidate position and the GNSS SPP measurement

$$W_{i,k}^{\text{GNSS}} = \exp\left[-\frac{1}{2} \left(\boldsymbol{p}_{i,k}^{-} - \boldsymbol{p}_i^{\text{GNSS}} \right)^{\text{T}} \boldsymbol{D}_{\text{GNSS},i}^{-1} \left(\boldsymbol{p}_{i,k}^{-} - \boldsymbol{p}_i^{\text{GNSS}} \right) \right], \tag{50}$$

where $\boldsymbol{D}_{\text{GNSS},i}$ denotes the covariance matrix used in the GNSS-proximity weighting term. In this study, $\boldsymbol{D}^{\text{GNSS}} = \text{diag}(5^2, 5^2)$ m^2 was used for both experimental routes.

The comprehensive candidate score is then calculated as

$$S_{i,k}^{C} = S_{i,k}^{\text{road}} \overline{S}_{i,k}^{\text{SM}} W_{i,k}^{\text{GNSS}}. \tag{51}$$

The comprehensive score is normalized as

$$\overline{S}_{i,k}^{\text{C}} = \frac{S_{i,k}^{\text{C}}}{\sum_{j=1}^{M_{\text{SM}}} S_{i,j}^{\text{C}}}. \tag{52}$$

Finally, the PDR-driven SM positioning result is calculated by weighted averaging

$$\boldsymbol{p}_i^{\text{PD-SM}} = \sum_{k=1}^{M_{\text{SM}}} \overline{S}_{i,k}^{\text{C}} \boldsymbol{p}_{i,k}^{-}. \tag{53}$$

The propagated candidate set provides the candidate-position input for the next epoch, while the normalized scores determine the current position estimate. At each subsequent epoch, the candidates are propagated using the new PDR displacement and evaluated using

the corresponding GNSS observations and map constraints. The 5 m initialization domain is applied only at the first epoch. It should be emphasized that although the method is inspired by particle propagation and weighting, it does not implement the complete prediction–weighting–resampling cycle of a standard PF. Therefore, it is referred to as PDR-driven candidate update SM rather than PF-PDR/SM.

Compared with standalone SM, the PDR-driven SM method introduces pedestrian motion continuity into the candidate update process. Compared with direct PDR/GNSS fusion, it evaluates candidate positions using environment-aware visibility information from the 3D building model. Therefore, this method can retain the cross-street constraint of SM while improving candidate discrimination along the walking direction.

3.4. Implementation Parameters and Controlled Comparison Settings

For reproducibility and controlled comparison, the implementation parameters used by the proposed and baseline methods are summarized in Table 2. All parameters were kept fixed for Routes 1 and 2, and no route-specific tuning was performed. The EKF-PDR/GNSS baseline and the proposed EKF-PDR/SM method used the same PDR measurements, state definition, initialization, and process-noise model. The PDR-derived step-length and heading uncertainties were set to 0.10 m and 5°, respectively. The two EKF methods differed only in the source and directional uncertainty of the absolute position update. GNSS SPP was modeled using an isotropic 10 m standard deviation, whereas the SM-derived observation was modeled in the heading frame using standard deviations of 20 m and 5 m in the along-heading and cross-heading directions, respectively. The PF-PDR/GNSS baseline used the same PDR uncertainty assumptions and GNSS measurement covariance as the EKF-PDR/GNSS baseline. All remaining SM and PDR-driven candidate parameters were also fixed across the two experimental routes.

The candidate-domain parameters listed in Table 2 serve different purposes and should be distinguished. Standalone SM uses a 30 m circular GNSS-centered search region at each positioning epoch. EKF-PDR/SM uses a ±10 m heading-orthogonal line-search range. In contrast, the 5 m radius in PDR-driven SM is used only to initialize the candidate set at the first epoch; subsequent candidates are propagated recursively using PDR-derived motion rather than being regenerated inside a GNSS-centered 5 m region.

The parameters listed in Table 2 also clarify the relationship between the proposed methods and the baseline methods. The EKF-PDR/SM method has the same state prediction structure as EKF-PDR/GNSS, but it replaces the raw GNSS SPP update with an SM-derived visibility measurement. The PDR-driven SM method uses candidate propagation and weighting concepts similar to PF-based fusion, but it does not perform particle resampling and uses SM visibility scoring as the main candidate evaluation mechanism.

The parameter settings in Table 2 combine literature-based model choices, analytically defined quantities, and fixed empirical implementation settings. The continuous C/N_0 scoring bounds follow [22], and the step-length model follows the Weinberg formulation [31]. The coefficient $K = 0.408$ was inherited from the existing PDR implementation, as explained in Section 2.2. Search ranges, candidate spacing, population sizes, smoothing strength, and uncertainty magnitudes were fixed implementation choices used consistently across both routes. They define the spatial support, numerical resolution, and relative weighting of the methods and are treated as study-specific settings.

The uncertainty settings also support the controlled comparison. The two EKF methods use the same initial covariance and PDR input uncertainties, while the PF baseline uses the same step-length, heading, and GNSS uncertainty assumptions. For the SM observation, the along-heading and cross-heading standard deviations of 20 m and 5 m produce a variance ratio of 16:1, expressing weaker along-heading information. The 5 m scale in the GNSS-

proximity term controls the spatial decay of candidate weights, whereas the 10 m GNSS standard deviation specifies the observation uncertainty used in the fusion baselines. These quantities serve different mathematical roles.

In the following experimental analysis, the proposed methods are compared with GNSS SPP, standalone SM, EKF-PDR/GNSS and PF-PDR/GNSS. This comparison is designed to examine whether the introduction of PDR constraints into visibility-based SM can improve the directional measurement stability of smartphone positioning in urban canyons.

Table 2. Key implementation parameters of the proposed and baseline positioning methods.

Module	Parameter	Value Used in This Study	Description
General settings	Coordinate frame	Local ENU	East and north components are used for horizontal positioning
	Route-specific tuning	None	The same parameters are used for Routes 1 and 2
Visibility-based SM	Initial candidate radius	30 m	Circular candidate region centered on GNSS SPP
	Candidate spacing	1 m	Grid interval for conventional SM candidate generation
	Road constraint	Enabled	Candidates outside the pedestrian-accessible road area are removed
	LOS-like C/N_0 threshold	31.91 dB-Hz	Upper signal-strength bound adopted from the continuous scoring configuration in [22]
	NLOS-like C/N_0 threshold	26.79 dB-Hz	Lower signal-strength bound adopted from the continuous scoring configuration in [22]
	Normalized score threshold	0.96	Retains candidates with min–max-normalized scores greater than 0.96; fixed for both routes within the local-optimization framework [21,22].
	SM position estimation	Score-weighted average	Retained candidate positions are averaged using their normalized SM scores
Common PDR settings	Step detection	Peak-valley detection	Applied to the tri-axial acceleration magnitude
	Step length model	Weinberg model	Fourth-root step-length model following [31]
	Weinberg coefficient K	0.408	Fixed coefficient for both experimental routes
	Heading source	Smartphone AHRS	Smartphone-derived heading angle
	Heading smoothing coefficient α_θ	0.80	First-order smoothing of the AHRS-derived heading
	Step-length standard deviation σ_L	0.10 m	PDR step-length uncertainty
	Heading standard deviation σ_θ	5° (0.0873 rad)	PDR heading uncertainty

Table 2. *Cont.*

Module	Parameter	Value Used in This Study	Description
Common EKF settings	State vector	$\boldsymbol{x}_i = [E_i, N_i]^{\mathrm{T}}$	Horizontal pedestrian position
	Control input	$\boldsymbol{u}_i = [L_i, \theta_i]^{\mathrm{T}}$	PDR-derived step length and heading
	Initial position	First valid GNSS SPP position	Common initialization for both EKF methods
	Initial covariance $\boldsymbol{P}_0$	$\mathrm{diag}(10^2, 10^2)$ m^2	Initial horizontal position uncertainty
	Process-noise covariance $\boldsymbol{Q}_i$	$\boldsymbol{G}_i \mathrm{diag}(0.10^2, 0.0873^2) \boldsymbol{G}_i^{\mathrm{T}}$	Propagation of step-length and heading uncertainties into position
	Position observation matrix $\boldsymbol{H}$	$\boldsymbol{I}_2$	Both EKF methods directly update horizontal position
EKF-PDR/GNSS baseline	PDR prediction model	Same as EKF-PDR/SM	Ensures identical motion prediction for controlled comparison
	Absolute observation	GNSS SPP position	Conventional GNSS/PDR position update
	GNSS measurement covariance $\boldsymbol{R}^{\mathrm{GNSS}}$	$\mathrm{diag}(10^2, 10^2)$ m^2	Isotropic 10 m standard deviation assigned to smartphone GNSS SPP
EKF-PDR/SM	PDR prediction model	Same as EKF-PDR/GNSS	Identical state prediction and process-noise model
	Candidate search direction	Heading-orthogonal	Perpendicular to smoothed PDR heading
	Candidate search range	±10 m	Search interval on both sides of the GNSS SPP position along the heading-orthogonal direction
	Candidate spacing	1 m	Spacing of heading-orthogonal SM candidates
	Absolute observation	SM-derived position	Environment-aware position update obtained from SM
	Along-heading SM standard deviation $\sigma_{\parallel}$	20 m	Weak along-heading constraint reflecting limited SM observability
	Cross-heading SM standard deviation $\sigma_{\perp}$	5 m	Stronger cross-heading constraint provided by building visibility
	SM covariance in heading frame $\boldsymbol{R}_h^{SM}$	$\mathrm{diag}(20^2, 5^2)$ m^2	Anisotropic SM measurement covariance
	SM covariance in EN frame $\boldsymbol{R}_i^{SM}$	$\boldsymbol{C}_i \boldsymbol{R}_h^{SM} \boldsymbol{C}_i^{\mathrm{T}}$	Heading-dependent covariance used in the EKF update
PF-PDR/GNSS baseline	State vector	$[E_i, N_i]^{\mathrm{T}}$	Horizontal position of each particle
	Number of particles M	1000	Fixed for both routes
	Initial particle distribution	2D Gaussian	Mean: first valid GNSS SPP position; covariance: $\mathrm{diag}(10^2, 10^2)$ m^2.
	Step-length perturbation	$N(0, 0.1^2)$ m	Same PDR step-length uncertainty as the EKF
	Heading perturbation	$N(0, 5^2)$ deg	Same PDR heading uncertainty as the EKF
	GNSS likelihood covariance	$\mathrm{diag}(10^2, 10^2)$ m^2	Same GNSS position uncertainty used in the EKF baseline
	Effective sample-size threshold	$N_{\mathrm{eff}} < 0.5M$	Resampling is triggered when particle degeneracy becomes significant
	Resampling strategy	Systematic resampling	Redistributes particles according to their normalized weights

Table 2. *Cont.*

Module	Parameter	Value Used in This Study	Description
PDR-driven SM	Initial candidate center	GNSS SPP position	Candidate set initialized around GNSS SPP
	Initial candidate radius	5 m	Circular truncation radius around the first-epoch GNSS SPP position
	Number of candidates	500	Fixed candidate population for both routes
	Initial candidate distribution	Truncated 2D Gaussian, $\sigma_E = \sigma_N = 2.5$ m	Samples outside the 5 m circular initialization domain are rejected and regenerated
	Candidate propagation	Step length + heading	Candidates are propagated using PDR displacement
	Step-length propagation noise	$\sigma_L = 0.1$ m	Independent zero-mean Gaussian step-length perturbation applied to each candidate at each detected step
	Heading propagation noise	$\sigma_\theta = 5°$	Independent zero-mean Gaussian heading perturbation applied to each candidate at each detected step
	Road constraint	Enabled	Candidates outside the road polygon receive zero weight
	GNSS-proximity covariance $\boldsymbol{D}^{\mathrm{GNSS}}$	$\mathrm{diag}(5^2, 5^2)$ m^2	Controls the GNSS-proximity weighting term
	Candidate score	$S_{i,k}^{\mathrm{road}} \overline{S}_{i,k}^{\mathrm{SM}} W_{i,k}^{\mathrm{GNSS}}$	Product of road validity, nonnegative normalized SM visibility score, and GNSS-proximity weight.
	Score normalization	$\sum_{k=1}^{M^{\mathrm{SM}}} \overline{S}_{i,k}^{C} = 1$	Normalized candidate weights used for position estimation
	Position estimation	Weighted average	Weighted mean of propagated candidate positions
	Resampling	Not used	Different from conventional particle filter

4. Experimental Configuration and Positioning Results

This section presents the experimental configuration and positioning results used to evaluate the proposed PDR-constrained SM methods in a building-obstructed campus environment containing both urban-canyon-like and relatively open pedestrian segments. The compared methods include GNSS pseudorange SPP, standalone SM, EKF-PDR/GNSS, PF-PDR/GNSS, EKF-PDR/SM and PDR-driven SM. The analysis is organized from qualitative trajectory comparison to directional error distributions and quantitative RMSE comparison.

4.1. Experimental Site and Measurement Configuration

The experiment was conducted in a building-obstructed campus environment at the School of Environment Science and Spatial Informatics, China University of Mining and Technology. A 3D building model constructed using oblique photogrammetry, together with the corresponding road-network information, was used to characterize the surrounding geometry and to support satellite visibility prediction, road-constrained candidate filtering, and reference-trajectory construction.

The 3D model and its derived reference trajectories are treated as geometric references with unquantified absolute uncertainty in this study. Relevant uncertainty sources include model georeferencing, reconstructed building and road geometry, reference-position selection, and temporal interpolation. The shared use of model geometry for SM constraints and

reference construction also introduces dependence between the positioning constraints and the evaluation reference.

As shown in Figure 5, the two routes represent distinctly different obstruction geometries. Along the principal section of Route 1, buildings on both sides of the pedestrian corridor are approximately 18–25 m high, while the effective separation between opposing building façades is approximately 13–16 m, corresponding to a representative building-height-to-street-width ratio H/W of approximately 1.6. This geometry produces continuous building obstruction on both sides of the route and is therefore treated as the urban-canyon-like test segment in this study. Route 2 is less confined: the route contains relatively open sections with wider surrounding clearances and a building-obstructed section where the adjacent buildings are approximately 15–25 m high and the effective opening width is approximately 20–35 m. Route 2 is therefore treated as an open-to-obstructed transition route rather than a uniformly severe urban canyon. These contrasting geometries provide two different levels of GNSS signal obstruction for evaluating the proposed methods.

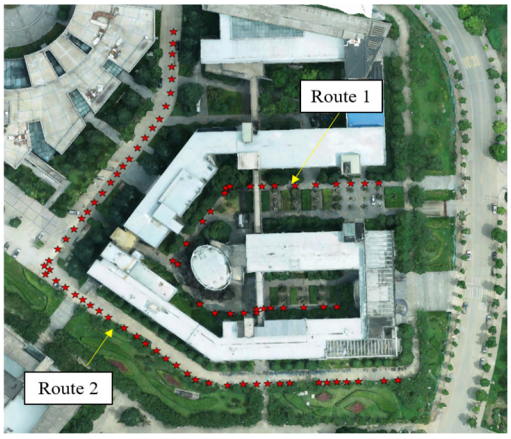


Figure 5. Experimental site, oblique-photogrammetry-based 3D building model, and pedestrian test routes. Route 1 represents the more continuously building-obstructed urban-canyon-like corridor, whereas Route 2 contains both relatively open and obstructed segments. The red stars indicate the pedestrian test routes.

A HUAWEI Mate 40 Pro smartphone (Huawei Device Co., Ltd., Dongguan, China) was used for all experiments. Both routes were traversed once by the same pedestrian using the same smartphone. GNSS Logger (Google, Android) and MATLAB Mobile (MathWorks, Android) were operated simultaneously to record GNSS raw measurements and smartphone inertial measurements, respectively. GNSS observations from GPS, BDS, Galileo, and GLONASS were used. The GNSS raw measurements were recorded at 1 Hz, whereas the inertial measurements used for PDR were recorded at 100 Hz.

The GNSS SPP positions used in this study were not obtained from the Android Location position output. Instead, pseudorange observations recorded by the GNSS Logger were processed offline using an iterative least-squares SPP solver. The primary-frequency code observations used in the processing were GPS L1 C/A, BDS B1I, Galileo E1, and GLONASS G1. Satellite positions and clock corrections were obtained from the corresponding broadcast navigation data. The resulting pseudorange SPP positions provided the raw absolute-position observations and the centers of the SM candidate regions.

Step events were detected on the high-rate inertial-data time axis and retained with their timestamps. The heading corresponding to each detected step was obtained from the temporally aligned smartphone attitude sequence. GNSS and PDR measurements were synchronized using their acquisition timestamps. For each 1 Hz GNSS epoch, all detected steps occurring after the preceding GNSS epoch and up to the current epoch

were sequentially applied for PDR state, particle, or candidate propagation. The GNSS- or SM-based absolute-position update was then performed at the corresponding GNSS epoch. The same synchronized GNSS epochs, detected steps, step-length estimates, and heading observations were used by all PDR-based methods.

The pedestrian maintained an approximately uniform walking speed during each traversal. Route 1 had a reference-trajectory length of 175 m and a walking duration of 180 s, yielding 181 synchronized positioning epochs and 275 detected steps. Route 2 was 287 m long and lasted 295 s, yielding 296 synchronized positioning epochs and 450 detected steps. Route lengths were calculated from the model-derived reference trajectories, and the epoch and step counts were restricted to the common synchronized evaluation intervals used by all compared methods.

The reference trajectories were derived from the oblique-photogrammetry-based 3D model rather than from an independent trajectory-recording device. Building and road-boundary coordinates were extracted from the model, and 29 reference positions were identified along Route 1 and 56 along Route 2. Temporal interpolation between these model-derived positions was used to obtain the reference position corresponding to each evaluated positioning epoch. Because no independent numerical survey accuracy was available for these reference trajectories, the reported directional errors and RMSEs represent deviations relative to the common model-derived reference trajectories rather than independently verified absolute geodetic accuracies.

All six positioning methods were evaluated using the same smartphone GNSS observations and model-derived reference trajectories. The same synchronized PDR inputs were supplied to all PDR-based methods, and the same 3D building model and road constraints were used by all SM-based methods. The implementation parameters listed in Table 2 were kept fixed for both routes without route-specific tuning. The experiment therefore provides a controlled within-dataset comparison of the relative behavior of the different positioning methods under the tested satellite-visibility conditions; its single-pedestrian, single-smartphone, and single-traversal scope is further discussed in Section 5.4.

4.2. Compared Methods and Evaluation Metrics

The compared methods were selected as representative and reproducible baselines from three related categories: raw smartphone GNSS positioning, visibility-based SM, and GNSS/PDR fusion.

(a) GNSS SPP: offline pseudorange single-point positioning computed from the smartphone raw GNSS measurements using the iterative least-squares solver described in Section 4.1, used as the basic absolute-positioning baseline [5–9];
(b) Standalone SM: visibility-based shadow matching using the 3D building model, road constraints and C/N_0-based scoring, representing conventional and smartphone-oriented SM methods [12–16,21,22];
(c) EKF-PDR/GNSS: EKF-based fusion of PDR prediction and GNSS SPP measurement, used as a conventional filtering baseline for smartphone GNSS/PDR integration [4,27];
(d) PF-PDR/GNSS: PF-based fusion of PDR propagation and GNSS SPP likelihood, used as a probabilistic GNSS/PDR fusion baseline related to smartphone GNSS/PDR fault detection and probabilistic integration methods [24];
(e) EKF-PDR/SM: the proposed EKF-based PDR/SM fusion method with heading-orthogonal SM candidate search, developed in this study to replace the raw GNSS update in EKF-PDR/GNSS with an SM-derived visibility measurement;
(f) PDR-driven SM: the proposed PDR-driven candidate update SM method, developed in this study to introduce PDR-based candidate propagation and GNSS-proximity weighting into visibility-based SM without particle resampling.

It should be noted that the EKF-PDR/GNSS and PF-PDR/GNSS methods are used as controlled baselines rather than exact reproductions of any single previously published algorithm. They are included to represent two common GNSS/PDR integration strategies—filtering-based fusion and probabilistic fusion—using the same synchronized GNSS and PDR inputs and the same reference trajectories. This controlled comparison allows the effect of replacing raw GNSS SPP updates with SM-derived visibility measurements to be evaluated without introducing differences in datasets, sensors or implementation details.

To examine the directional measurement behavior of different methods, the horizontal positioning error was decomposed into along-street and cross-street components. Let $\boldsymbol{p}_i^{\mathrm{ref}}$ denote the temporally interpolated model-derived reference position at epoch i, as described in Section 4.1, and let $\boldsymbol{p}_i^{\mathrm{est}}$ denote the estimated position of a given method. The horizontal error vector is

$$\boldsymbol{e}_i = \boldsymbol{p}_i^{\mathrm{est}} - \boldsymbol{p}_i^{\mathrm{ref}}. \tag{54}$$

The along-street unit vector is determined from the local direction of the reference trajectory

$$\boldsymbol{u}_i^{\parallel} = \frac{\boldsymbol{p}_{i+1}^{\mathrm{ref}} - \boldsymbol{p}_{i-1}^{\mathrm{ref}}}{\left\| \boldsymbol{p}_{i+1}^{\mathrm{ref}} - \boldsymbol{p}_{i-1}^{\mathrm{ref}} \right\|}. \tag{55}$$

The cross-street unit vector is defined as

$$\boldsymbol{u}_i^{\perp} = \begin{bmatrix} \boldsymbol{u}_{N,i}^{\parallel} \\ -\boldsymbol{u}_{E,i}^{\parallel} \end{bmatrix}, \tag{56}$$

where $\boldsymbol{u}_{E,i}^{\parallel}$ and $\boldsymbol{u}_{N,i}^{\parallel}$ are the east and north components of $\boldsymbol{u}_i^{\parallel}$, respectively. The absolute along-street and cross-street errors are then calculated as

$$d_i^{\parallel} = \left| \boldsymbol{e}_i^{\mathrm{T}} \boldsymbol{u}_i^{\parallel} \right|, \tag{57}$$

$$d_i^{\perp} = \left| \boldsymbol{e}_i^{\mathrm{T}} \boldsymbol{u}_i^{\perp} \right|. \tag{58}$$

The positioning performance was evaluated using directional cumulative distribution functions (CDFs) and root mean square error (RMSE). The CDFs characterize the overall distribution of positioning errors, whereas RMSE provides a compact quantitative measure of the overall error magnitude. For an error sequence d_i, the RMSE is calculated as

$$RMSE = \sqrt{\frac{1}{n} \sum_{i=1}^{n} d_i^2}, \tag{59}$$

where n is the number of evaluated epochs. The same metrics were calculated separately for the along-street and cross-street error components.

4.3. Qualitative Trajectory Comparison

Figure 6 shows the trajectory-level comparison on Route 1. In this route, GNSS measurements were strongly affected by the surrounding buildings, and the standalone SM result suffered from road-mismatching in some epochs. This indicates that although SM can use 3D visibility information to constrain the candidate positions, its performance may become unstable when smartphone C/N_0 measurements fluctuate under severe signal obstruction.

Compared with standalone SM, the proposed EKF-PDR/SM and PDR-driven SM methods show improved trajectory continuity. The PDR constraint helps suppress unreasonable jumps and reduces the risk of road-mismatching. Compared with the PDR/GNSS baselines, the proposed methods reduce direct dependence on raw GNSS SPP. EKF-PDR/SM uses GNSS SPP to center its candidate search and employs the resulting SM position as the EKF observation. After initialization, PDR-driven SM incorporates current GNSS SPP

through a proximity-weighting term while evaluating propagated candidates using visibility information.

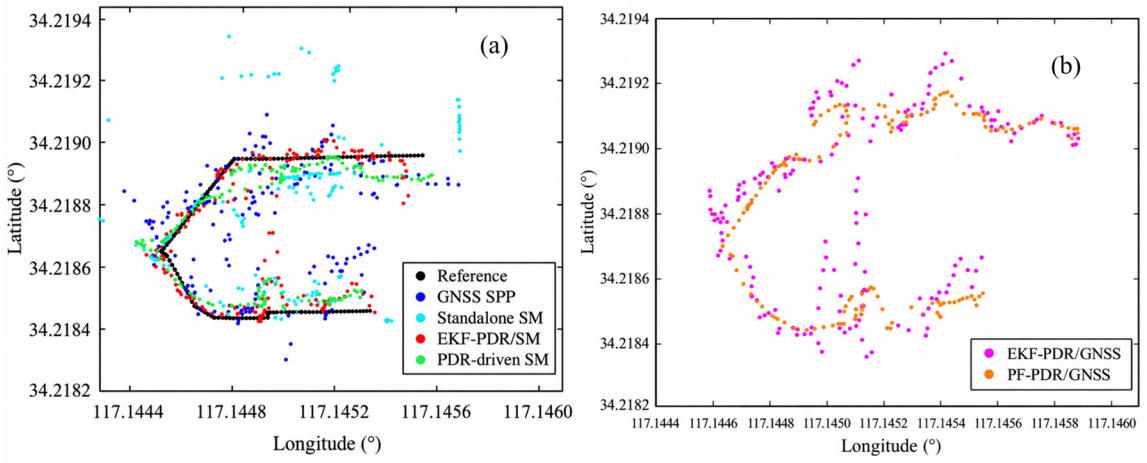


Figure 6. Qualitative trajectory comparison on Route 1: (**a**) GNSS SPP, standalone SM and proposed PDR-constrained SM methods; (**b**) EKF-PDR/GNSS and PF-PDR/GNSS baselines.

Figure 7 shows the trajectory-level comparison on Route 2. Unlike Route 1, Route 2 contains both relatively open and obstructed segments. Therefore, the performance of different methods is more dependent on the local satellite visibility condition. In relatively open areas, PDR/GNSS fusion can benefit from more reliable GNSS SPP updates. In urban-canyon segments, however, raw GNSS SPP may become biased, and the SM-derived visibility measurement can provide additional environmental constraints.

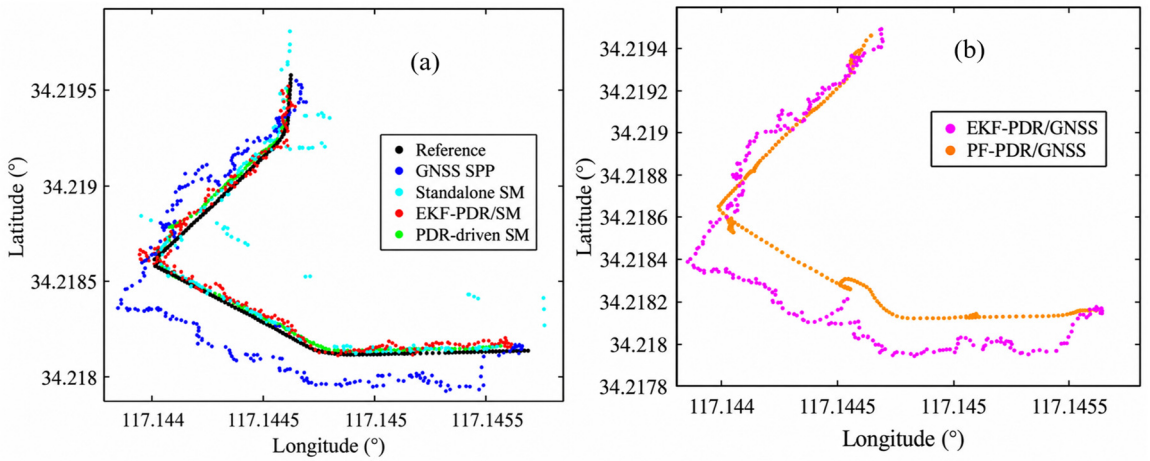


Figure 7. Qualitative trajectory comparison on Route 2: (**a**) GNSS SPP, standalone SM and proposed PDR-constrained SM methods; (**b**) EKF-PDR/GNSS and PF-PDR/GNSS baselines.

The trajectory comparison suggests that the advantage of PDR-constrained SM is related to the degradation level of GNSS pseudorange positioning. When raw GNSS SPP is unreliable, using visibility-based SM as an environment-aware measurement update can reduce the influence of biased GNSS observations. When GNSS SPP is relatively stable, direct PDR/GNSS fusion may also provide competitive results. Therefore, the following subsections further evaluate the methods using directional CDFs and RMSE values.

4.4. Directional Error Cumulative Distributions

The directional CDFs on Route 1 are shown in Figure 8. The cross-street CDFs evaluate the ability of different methods to identify the correct side of the street, while the along-street CDFs evaluate the ability to control errors along the walking direction.

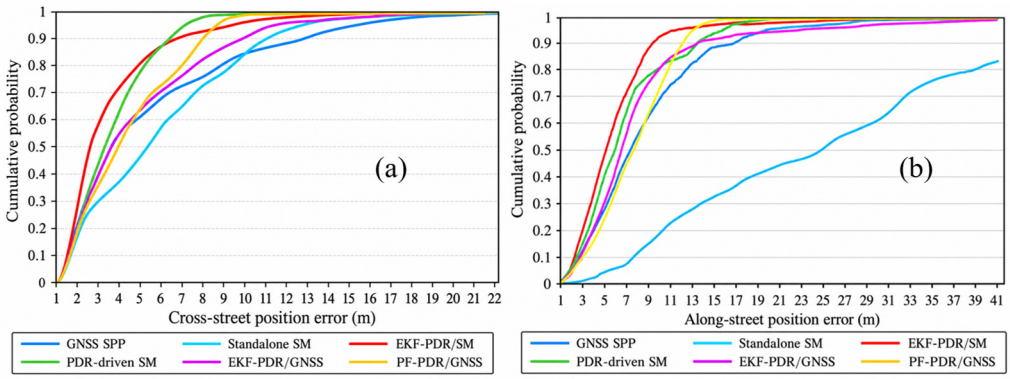


Figure 8. Directional error cumulative distributions on Route 1: (**a**) cross-street errors; (**b**) along-street errors.

For Route 1, the EKF-PDR/SM configuration produces a clear leftward shift in the cross-street error distribution relative to EKF-PDR/GNSS. In the along-street direction, EKF-PDR/SM also provides a modest improvement, reducing the RMSE from 8.98 m to 8.28 m, corresponding to a reduction of 7.8%. The smaller improvement in the along-street direction compared with the cross-street direction is consistent with the anisotropic SM measurement model, in which substantially lower confidence is assigned to the SM observation along the pedestrian heading.

Figure 9 shows the directional CDFs on Route 2. For Route 2, EKF-PDR/SM improves both directional error distributions relative to EKF-PDR/GNSS. The relative RMSE reduction is larger in the cross-street component. The along-street improvement reflects the joint effects of PDR prediction, anisotropic measurement weighting, and trajectory evolution, consistent with the limited direct along-street discrimination of SM.

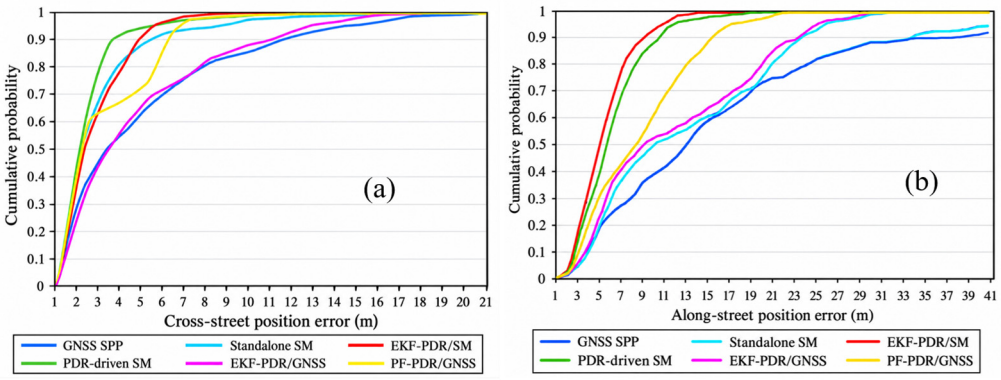


Figure 9. Directional error cumulative distributions on Route 2: (**a**) cross-street errors; (**b**) along-street errors.

For Route 2, the standalone SM method still shows limited along-street improvement, but its cross-street performance becomes more stable in some segments because the visibility geometry is less severely degraded than that in Route 1. The proposed PDR-constrained SM methods provide improved directional error control, but their advantages differ between cross-street and along-street components. This indicates that the two proposed methods have different measurement characteristics: EKF-PDR/SM is more suitable for

filtering-based position updates, whereas PDR-driven SM is more focused on candidate-level propagation and score discrimination.

4.5. Directional RMSE Comparison

The directional RMSEs of all compared positioning methods on Routes 1 and 2 are summarized in Table 3. Lower RMSE values indicate better overall positioning performance in the corresponding direction.

Table 3. Directional RMSEs of the compared positioning methods on Routes 1 and 2.

Method	Route 1		Route 2	
	Cross-Street RMSE (m)	Along-Street RMSE (m)	Cross-Street RMSE (m)	Along-Street RMSE (m)
GNSS SPP	6.61	9.50	5.89	14.40
Standalone SM	6.76	28.55	5.30	18.44
EKF-PDR/GNSS	5.23	8.98	4.29	12.38
PF-PDR/GNSS	4.02	7.71	2.64	9.20
EKF-PDR/SM	3.57	8.28	2.46	7.83
PDR-driven SM	2.92	7.47	1.54	5.89

On Route 1, standalone SM exhibits a particularly large along-street RMSE of 28.55 m, confirming its weak observability along the street direction under severely degraded GNSS conditions. Under the controlled EKF configuration, EKF-PDR/SM reduces the cross-street RMSE from 5.23 m for EKF-PDR/GNSS to 3.57 m, corresponding to a reduction of 31.7%. The along-street RMSE is also reduced from 8.98 m to 8.28 m, corresponding to a modest improvement of 7.8%. This improvement is substantially smaller than the 31.7% reduction in the cross-street RMSE, which is consistent with the anisotropic SM measurement model: the SM-derived observation provides a stronger cross-street constraint, whereas its direct influence in the along-heading direction is deliberately limited. PDR-driven SM achieves the lowest RMSEs on Route 1, with cross-street and along-street values of 2.92 m and 7.47 m, respectively.

On Route 2, EKF-PDR/SM reduces the cross-street RMSE from 4.29 m for EKF-PDR/GNSS to 2.46 m, corresponding to an improvement of 42.7%. The along-street RMSE is also reduced from 12.38 m to 7.83 m, representing an improvement of 36.8%. This along-street improvement is interpreted in terms of the combined PDR prediction, directional observation weighting, and trajectory geometry. In particular, the larger along-heading SM observation uncertainty changes the influence of the GNSS-centered along-heading coordinate in the EKF update. PDR-driven SM again provides the lowest directional RMSEs, reaching 1.54 m in the cross-street direction and 5.89 m in the along-street direction.

Overall, Table 3 and Figures 8 and 9 describe the comparative performance of six complete positioning configurations. EKF-PDR/SM and PDR-driven SM are evaluated as full pipelines, including their motion inputs, GNSS-derived constraints, and visibility processing. The resulting RMSE differences characterize complete-configuration performance under the tested conditions.

5. Discussion

The experimental results demonstrate that introducing PDR measurements into visibility-based SM can improve smartphone positioning performance on the two tested campus routes. This section further discusses the measurement mechanism behind the

observed improvements, the influence of GNSS degradation, the difference between the two proposed PDR-constrained SM methods and the limitations of the present study.

5.1. Directional Complementarity Between SM and PDR

The results confirm that visibility-based SM and PDR have complementary directional measurement characteristics. Standalone SM uses 3D building-model-aided satellite visibility information to evaluate candidate positions, which is particularly useful for distinguishing positions on different sides of a street. Therefore, SM can provide an effective cross-street constraint when the surrounding buildings produce clear satellite visibility differences. However, candidate positions along the same street may share similar visibility patterns, resulting in weak along-street discrimination.

The controlled EKF comparison illustrates this directional complementarity. On Route 1, EKF-PDR/SM reduces the cross-street RMSE from 5.23 m for EKF-PDR/GNSS to 3.57 m, corresponding to a reduction of 31.7%, whereas the along-street RMSE decreases more modestly from 8.98 m to 8.28 m, corresponding to a reduction of 7.8%. The larger relative improvement in the cross-street direction is consistent with the directional discrimination of visibility-based SM. The along-street change reflects the combined influence of PDR propagation, direction-dependent observation weighting, and two-dimensional trajectory evolution.

On Route 2, EKF-PDR/SM reduces the cross-street RMSE from 4.29 m to 2.46 m and the along-street RMSE from 12.38 m to 7.83 m. The latter improvement does not imply strong direct along-street observability from SM. The heading-orthogonal search retains the GNSS-centered along-heading coordinate, and the EKF assigns that component a 20 m observation standard deviation. The Route 2 along-street result therefore reflects the complete fusion configuration, including PDR prediction, anisotropic observation weighting, and changes in heading and covariance along the route. PDR supplies motion continuity, while visibility scoring primarily distinguishes cross-heading candidate positions.

5.2. Effect of GNSS Degradation on Fusion Performance

The comparison with EKF-PDR/GNSS and PF-PDR/GNSS baselines shows that the choice of absolute measurement update is critical in urban canyons. Direct PDR/GNSS fusion uses raw GNSS SPP as the absolute update. When GNSS SPP is moderately reliable, this strategy can effectively correct PDR drift. However, when GNSS pseudorange positioning is strongly biased by NLOS reception and multipath effects, direct fusion with GNSS SPP may introduce erroneous absolute updates into the trajectory.

This explains why the proposed PDR-constrained SM methods are advantageous in degraded GNSS conditions. Instead of directly using GNSS SPP as the position update, the proposed methods reinterpret GNSS signal reception through 3D building-model-aided visibility consistency. In this way, the raw GNSS measurements are transformed into an environment-aware visibility measurement. This mechanism can reduce the influence of biased pseudorange positioning, especially when satellite blockage and NLOS reception are severe.

The Route 1 results support this interpretation. Under identical PDR prediction and process-noise settings, EKF-PDR/SM reduces the cross-street RMSE from 5.23 m for EKF-PDR/GNSS to 3.57 m. This comparison indicates that replacing raw GNSS SPP updates with the directionally weighted SM-derived observation provides a stronger cross-street constraint under severe GNSS degradation.

The close agreement between the PF trajectory and the reference on the eastern leg of Route 2 is interpreted as the local performance of that configuration. The plotted agreement describes the combined filter behavior; quantifying the respective contributions of PDR propagation and GNSS updates requires a separate component-level comparison. Table 3

and Figures 8 and 9 provide the full-route comparisons used here. These comparisons support relative-performance conclusions for the complete proposed methods against the evaluated baselines under the tested conditions.

5.3. Difference Between EKF-PDR/SM and PDR-Driven SM

Although both proposed methods integrate PDR with visibility-based SM, their measurement mechanisms are different.

The EKF-PDR/SM method is a filtering-based fusion strategy. It first uses the PDR-derived heading to reshape the SM candidate domain into a heading-orthogonal line search. The resulting SM-derived position is then introduced into the EKF using a heading-dependent anisotropic covariance. The along-heading standard deviation is set to 20 m, substantially larger than the 5 m cross-heading standard deviation. Consequently, the EKF deliberately assigns much lower confidence to the SM observation along the walking direction. The direct role of SM is therefore concentrated on cross-street correction, whereas along-trajectory continuity is primarily maintained by PDR prediction.

The results in Table 3 are consistent with this directional design. The along-street benefits are interpreted as outcomes of the combined PDR prediction, anisotropic measurement weighting, and trajectory evolution, while the direct spatial discrimination of visibility scoring remains concentrated across the heading direction.

The PDR-driven SM method is a candidate-level measurement enhancement strategy. Instead of generating independent candidate regions at each epoch, it propagates candidate positions using PDR-derived step length and heading. Candidate positions are then evaluated using both visibility consistency and GNSS-proximity weighting. This design helps maintain candidate continuity and enlarge score differences among candidates, especially in the cross-street direction. Across the two routes, PDR-driven SM achieves the lowest directional RMSEs among all compared methods, with cross-street/along-street RMSEs of 2.92/7.47 m on Route 1 and 1.54/5.89 m on Route 2.

Therefore, the two methods should be regarded as complementary implementations of PDR-constrained SM rather than as equivalent fusion strategies. EKF-PDR/SM provides a filtering-based mechanism that explicitly incorporates the directional uncertainty of SM and primarily strengthens the cross-street constraint. In contrast, PDR-driven SM introduces pedestrian motion directly at the candidate-propagation and scoring levels and achieves lower directional RMSEs in the present experiments. These different behaviors demonstrate that PDR information can be incorporated into visibility-based SM at either the measurement-update level or the candidate-propagation level, with different trade-offs in filtering structure, candidate continuity, and directional positioning performance.

5.4. Scope and Limitations of the Experimental Validation

The present experiments were designed primarily to examine the relative behavior of PDR-constrained SM under two representative satellite-visibility conditions rather than to provide an exhaustive benchmark across devices, pedestrians, and urban environments. The validation was conducted using one pedestrian, one smartphone model, and one traversal of each of the two experimental routes, with 29 and 56 model-derived reference positions used for Route 1 and Route 2, respectively. Therefore, the reported error statistics should be interpreted as evidence under the tested device, route, and visibility conditions rather than as universal performance bounds of the proposed methods. Accordingly, the reported statistics represent controlled single-traversal experiments rather than repeated-trial population statistics. A further limitation concerns the reference trajectory. The evaluated reference positions were derived from the oblique-photogrammetry-based 3D model and temporally interpolated to the positioning epochs, rather than being obtained from an

independently surveyed centimeter-level trajectory. Therefore, the reported meter-level RMSEs should be interpreted as relative errors with respect to this common model-derived reference trajectory. In particular, the lowest cross-street RMSE values of approximately 1–2 m should not be interpreted as independently verified absolute geodetic accuracies at the same level.

The controlled experimental design provides a consistent basis for relative comparison. All six methods were evaluated using the same GNSS observations and reference trajectories; all PDR-based methods used the same synchronized motion inputs, and all SM-based methods used the same 3D building model and road constraints. Algorithmic settings were maintained across the two routes without route-specific tuning. The two routes represent substantially different satellite visibility conditions, allowing the directional behavior of the proposed methods to be evaluated under both severe and moderate GNSS degradation. Further experiments involving repeated traversals, additional pedestrians, different smartphone models, and more diverse urban geometries are required to assess the broader generalizability of the framework.

The tested environment represents a campus-scale building-obstruction scenario, with Route 1 providing the stronger urban-canyon-like geometry and Route 2 providing an open-to-obstructed transition. Therefore, the present results should not be interpreted as an exhaustive validation across high-rise downtown street canyons with substantially larger H/W ratios.

The comparison in this study comprises six complete GNSS/SM-based configurations. Quantifying the incremental benefit of SM over open-loop motion requires a PDR-only baseline with matched initialization, motion inputs, and evaluation epochs. That incremental benefit remains unquantified in the present experiments; the claims are therefore restricted to the comparative performance of the complete evaluated configurations.

5.5. Relation to Previous Studies and Potential Extensions

Previous studies provide useful context for interpreting the present results. Wang et al. [14] demonstrated the cross-street benefit of smartphone shadow matching, while Hsu et al. [23] integrated smartphone PDR with 3D map-aided GNSS and reported positioning errors of approximately 1.5 m and 5.5 m in middle-class and deep urban canyons, respectively. The directional results in Table 3 further examine this complementarity by distinguishing cross-street visibility constraints from along-trajectory motion continuity. The heading-orthogonal search and anisotropic SM covariance explicitly represent this directional difference, while PDR-driven candidate propagation introduces temporal continuity into SM. These studies provide methodological and performance context; their numerical results are interpreted within their respective devices, environments, reference systems, and error definitions.

Deep learning provides a further direction for improving measurement-quality modeling. Recent Transformer-based research has used satellite spatial characteristics to predict visibility and GNSS measurement uncertainty [32]. Within the present framework, learned visibility probabilities provide a potential input to candidate scoring, while predicted measurement uncertainty provides a basis for adapting the relative confidence assigned to GNSS and SM information. This extension targets variations in signal quality across environments and smartphone conditions. Its contribution to positioning accuracy requires evaluation using independent training and testing data, together with assessment of cross-device transfer, uncertainty calibration, and computational cost.

Potential applications include smartphone pedestrian guidance, campus navigation, and location-based services in mapped urban districts. The framework combines pedestrian motion continuity with building-based visibility constraints to support positioning near

obstructing structures. Practical deployment requires suitable 3D building and pedestrian-accessibility information, timestamp-aligned sensor measurements, and validation under the intended device and carrying conditions. These requirements define a clear path from the present campus experiments to broader pedestrian applications.

6. Conclusions

This paper proposed a PDR-constrained GNSS shadow matching framework for improving smartphone pedestrian positioning in urban canyons. The study was motivated by the directional limitation of visibility-based shadow matching, which can provide useful cross-street constraints through 3D building-model-aided satellite visibility measurements but generally suffers from weak along-street observability in dynamic pedestrian applications. To exploit the complementary measurement characteristics of SM and PDR, two PDR-constrained SM methods were developed.

The first method, EKF-PDR/SM, uses PDR-derived heading measurements to constrain SM candidate generation along a heading-orthogonal direction and then fuses the SM-derived position with PDR prediction in an EKF framework. The second method, PDR-driven SM, propagates candidate positions using PDR-derived step length and heading measurements and evaluates the propagated candidates using both visibility consistency and GNSS-proximity weighting. These two methods introduce pedestrian motion information into visibility-based SM at different levels: measurement-update level and candidate-propagation level.

Experiments were conducted on two pedestrian routes with different satellite-visibility conditions in a building-obstructed campus environment. The proposed methods were compared with GNSS SPP, standalone SM, EKF-PDR/GNSS and PF-PDR/GNSS using directional CDFs and RMSE. The results show that standalone SM can suffer from along-street ambiguity and road-mismatching under degraded GNSS conditions. Under the controlled EKF comparison using identical PDR prediction and process-noise settings, EKF-PDR/SM reduced the cross-street RMSE from 5.23 m to 3.57 m on Route 1 and from 4.29 m to 2.46 m on Route 2. In the along-street direction, the RMSE decreased more modestly from 8.98 m to 8.28 m on Route 1 and from 12.38 m to 7.83 m on Route 2. These results are consistent with the cross-street visibility discrimination of SM and the motion continuity supplied by PDR. Along-street performance reflects the combined fusion configuration, including PDR propagation, directional measurement weighting, and trajectory geometry.

On the two tested campus routes, the complete PDR-constrained SM configurations achieved the reported directional RMSEs relative to the evaluated GNSS/SM-based baselines. EKF-PDR/SM combines motion prediction with a heading-dependent SM observation, whereas PDR-driven SM combines candidate propagation, visibility scoring, and GNSS-proximity weighting. These results provide within-dataset evidence for the comparative performance of the complete configurations. The incremental gain of SM over matched PDR-only propagation remains an additional question for component-level evaluation.

Future work will extend the validation to longer trajectories, more diverse urban environments, multiple smartphone models and different carrying modes. Further analysis of parameter sensitivity, 3D model accuracy and direct comparison with ray-tracing-based 3D map-aided GNSS/PDR methods will also be conducted to evaluate the broader applicability of the proposed framework.

Author Contributions: Conceptualization, N.Q., X.H., G.C. and J.G.; methodology, N.Q., X.H. and G.C.; software, X.H., Y.C. and H.L.; validation, X.H., Y.L. and Y.C.; formal analysis, N.Q. and X.H.; investigation, X.H., Y.L. and Y.C.; resources, G.C., J.G., Y.F. and Y.H.; data curation, X.H., Y.C. and H.L.; writing—original draft preparation, N.Q. and X.H.; writing—review and editing, N.Q., G.C., J.G., Y.L., Y.F. and Y.H.; visualization, X.H., Y.C. and H.L.; supervision, G.C. and J.G.; project administration,

N.Q. and G.C.; funding acquisition, N.Q., G.C. and J.G. All authors have read and agreed to the published version of the manuscript.

Funding: This work was supported by the National Natural Science Foundation of China (Grant No. 42504028), the Basic Research Program of Jiangsu Province (Grant No. BK20241665), the Fundamental Research Funds for the Central Universities (Grant Nos. 2024ZDPYCH1003 and 2025QN1109), and the Open Foundation of Tianjin Key Laboratory of Rail Transit Navigation Positioning and Spatio-temporal Big Data Technology (Grant No. TKL2025B01).

Institutional Review Board Statement: Not applicable.

Informed Consent Statement: Not applicable.

Data Availability Statement: The data supporting the findings of this study are available from the corresponding author upon reasonable request.

Conflicts of Interest: The authors declare no conflicts of interest.

References

1. Liu, J.; Gao, K. Challenges and opportunities for mapping and surveying and location-based service in the age of intelligence. *J. Geomat. Inf. Sci. Wuhan Univ.* **2017**, *42*, 1506–1517.
2. Chen, L.; Thombre, S.; Järvinen, K.; Lohan, E.S.; Alén-Savikko, A.; Leppäkoski, H.; Bhuiyan, M.Z.H.; Bu-Pasha, S.; Ferrara, G.N.; Honkala, S.; et al. Robustness, security and privacy in location-based services for future IoT: A survey. *IEEE Access* **2017**, *5*, 8956–8977. [CrossRef]
3. Wang, J.; Liu, F.; Han, H.; Li, Z.; Wang, X.; Zhang, Y. Key technologies and applications of high-precision positioning in surveying and navigation. *Navig. Position. Timing* **2020**, *7*, 1–11.
4. Zhang, J.; Yu, B.; Ge, Y.; Gao, J.; Sheng, C. An effective GNSS/PDR fusion positioning algorithm on smartphones for challenging scenarios. *Sensors* **2024**, *24*, 1452. [CrossRef] [PubMed]
5. Zhu, N.; Marais, J.; Betaille, D.; Berbineau, M. GNSS position integrity in urban environments: A review of literature. *IEEE Trans. Intell. Transp. Syst.* **2018**, *19*, 2762–2778. [CrossRef]
6. Wang, F.; Luan, M.; Cheng, Y.; Zhu, H.; Zhao, G.; Zhang, W. Smartphone GNSS/MEMS IMU tightly-coupled integration positioning method for vehicular navigation in urban conditions. *J. Geomat. Inf. Sci. Wuhan Univ.* **2023**, *48*, 1106–1116.
7. Zhang, X.; Tao, X.; Wang, Y.; Liu, W.; Zhu, F. MEMS-enhanced smartphone GNSS high-precision positioning for vehicular navigation in urban conditions. *J. Geomat. Inf. Sci. Wuhan Univ.* **2022**, *47*, 1740–1749.
8. Zhang, K.; Jiao, W.; Li, J. Analysis of GNSS positioning precision on Android smart devices. *J. Geomat. Inf. Sci. Wuhan Univ.* **2019**, *44*, 1472–1477.
9. Ge, Y.; Liu, Z.; Li, Z.; Wang, Y.; Liu, B. Analysis of stochastic models and smoothing methods in smartphone single point positioning. *J. Hefei Univ. Technol.* **2022**, *45*, 1113–1119.
10. Wu, Q.; Sun, M.; Zhou, C.; Zhang, P. Precise point positioning using dual-frequency GNSS observations on smartphone. *Sensors* **2019**, *19*, 2189. [CrossRef] [PubMed]
11. Liu, C.; Gao, J.; Yu, Z.; Wang, J. An optimal pseudolites location model of GPS/pseudolites integrated relative positioning. *J. China Univ. Min. Technol.* **2012**, *41*, 120–126.
12. Groves, P.D. Shadow matching: A new GNSS positioning technique for urban canyons. *J. Navig.* **2011**, *64*, 417–430. [CrossRef]
13. Wang, L.; Groves, P.D.; Ziebart, M.K. GNSS shadow matching: Improving urban positioning accuracy using a 3D city model with optimized visibility scoring scheme. *J. Inst. Navig.* **2013**, *60*, 195–207. [CrossRef]
14. Wang, L.; Groves, P.D.; Ziebart, M.K. Smartphone shadow matching for better cross-street GNSS positioning in urban environments. *J. Navig.* **2015**, *68*, 411–433. [CrossRef]
15. Groves, P.D.; Wang, L.; Adjrad, M.; Ellul, C. GNSS shadow matching: The challenges ahead. In Proceedings of the ION GNSS+ Conference, Tampa, FL, USA, 14–18 September 2015; pp. 2421–2443.
16. Luo, H.; Weng, D.; Chen, W. An improved shadow matching method for smartphone positioning. *J. Geomat. Inf. Sci. Wuhan Univ.* **2021**, *46*, 1907–1915.
17. Hsu, L.T.; Gu, Y.; Kamijo, S. 3D building model-based pedestrian positioning method using GPS/GLONASS/QZSS and its reliability calculation. *GPS Solut.* **2016**, *20*, 413–428. [CrossRef]
18. Wang, S.; Zhang, B.; Yin, M. Research on shadow matching algorithm for GNSS positioning of mobile terminal based on dynamic threshold. *J. Geod. Geodyn.* **2021**, *41*, 1101–1105.
19. Sun, R.; Hsu, L.-T.; Xue, D.; Zhang, G.; Ochieng, W.Y. GPS signal reception classification using adaptive neuro-fuzzy inference system. *J. Navig.* **2019**, *72*, 685–701. [CrossRef]

20. Zhang, G.; Wen, W.; Hsu, L.T. Rectification of GNSS-based collaborative positioning using 3D building models in urban areas. *GPS Solut.* **2019**, *23*, 83. [CrossRef]
21. Hu, Y.; Li, Z.; Sun, J.; Ge, Y.; Shao, K.; Wang, Y. Smartphone GNSS Shadow Matching Algorithm Considering Local Optimal. *J. Geomat. Inf. Sci. Wuhan Univ.* **2025**, *50*, 856–865.
22. Han, X.; Qian, N.; Gao, J.; Li, Z.; Hu, Y.; Yang, L.; Li, F. An enhanced local optimization algorithm for GNSS shadow matching in mobile phones. *Remote Sens.* **2025**, *17*, 677. [CrossRef]
23. Hsu, L.-T.; Gu, Y.; Huang, Y.; Kamijo, S. Urban pedestrian navigation using smartphone-based dead reckoning and 3-D map-aided GNSS. *IEEE Sens. J.* **2016**, *16*, 1281–1293. [CrossRef]
24. Jiang, C.; Chen, Y.; Liu, Z.; Xia, Q.; Chen, C.; Hyyppa, J. A probabilistic method-based smartphone GNSS fault detection and exclusion system utilizing PDR step length. *Remote Sens.* **2023**, *15*, 4993. [CrossRef]
25. Jiang, C.; Chen, Y.; Chen, C.; Jia, J.; Sun, H.; Wang, T.; Hyyppa, J. Smartphone PDR/GNSS integration via factor graph optimization for pedestrian navigation. *IEEE Trans. Instrum. Meas.* **2022**, *71*, 8504112. [CrossRef]
26. Wang, J.; Mi, X.; Chen, W.; Luo, H.; Mansour, A.; Li, Y.; Yu, Y.; Weng, D. Tightly coupled Bluetooth enhanced GNSS/PDR system for pedestrian navigation in dense urban environments. *IEEE Trans. Instrum. Meas.* **2024**, *73*, 9519713. [CrossRef]
27. Magsi, A.H.; Díez, L.E. Comparison of FGO and KF for PDR-GNSS fusion under different PDR errors. *IEEE Trans. Instrum. Meas.* **2024**, *73*, 8506312. [CrossRef]
28. Zhang, G.; Wen, W.; Xu, B.; Hsu, L.-T. Extending shadow matching to tightly-coupled GNSS/INS integration system. *IEEE Trans. Veh. Technol.* **2020**, *69*, 4979–4991. [CrossRef]
29. Zhang, J.; Wen, W.; Huang, F.; Wang, Y.; Chen, X.; Hsu, L.-T. GNSS-RTK adaptively integrated with LiDAR/IMU odometry for continuously global positioning in urban canyons. *Appl. Sci.* **2022**, *12*, 5193. [CrossRef]
30. Jin, Z.; Li, Y.; Yang, Z.; Zhang, Y.; Cheng, Z. Real-time indoor positioning based on BLE beacons and pedestrian dead reckoning for smartphones. *Appl. Sci.* **2023**, *13*, 4415. [CrossRef]
31. Weinberg, H. *Using the ADXL202 in Pedometer and Personal Navigation Applications*; Application Note AN-602; Analog Devices, Inc.: Norwood, MA, USA, 2002.
32. Zhang, Z.; Xu, P.; Zhang, G. Intelligent urban GNSS measurement uncertainty prediction by exploring the spatial characteristics with transformer. *Appl. Soft Comput.* **2025**, *184*, 113773. [CrossRef]

Disclaimer/Publisher's Note: The statements, opinions and data contained in all publications are solely those of the individual author(s) and contributor(s) and not of MDPI and/or the editor(s). MDPI and/or the editor(s) disclaim responsibility for any injury to people or property resulting from any ideas, methods, instructions or products referred to in the content.